**PERSPECTIVE**

Check for updates

# ZIF-8 metal–organic frameworks and their hybrid materials: emerging photocatalysts for energy and environmental applications

Diptirani Behera, Priyanka Priyadarshini and Kulamani Parida ⓘ *

In the face of escalating environmental challenges such as fossil fuel dependence and water pollution, innovative solutions are essential for sustainable development. In this regard, zeolitic imidazolate frameworks (ZIFs), specifically ZIF-8, act as promising photocatalysts for environmental remediation and renewable energy applications. ZIF-8, a subclass of metal–organic frameworks (MOFs), is renowned for its large specific surface area, high porosity, rapid electron transfer ability, abundant functionalities, ease of designing, controllable properties, and remarkable chemical and thermal stability. However, its application as a standalone photocatalyst is limited by issues such as particle aggregation, poor water stability, and insufficient visible light absorption. By integrating ZIF-8 with various photoactive materials to form composite catalysts, these drawbacks can be mitigated, leading to enhanced photocatalytic efficiency. The review discusses the synthesis, properties, and applications of ZIF-8-based photocatalysts in light-driven $H_2$ evolution, $H_2O_2$ evolution, $CO_2$ reduction, and dye and drug degradation. It also highlights the challenges and future research directions in developing cost-effective, scalable, and environmentally friendly ZIF-8 composites for industrial applications. The potential of ZIF-8 composites to contribute to sustainable global energy solutions and environmental cleanup is significant, yet further exploration is required to harness their capabilities thoroughly.

## 1. Introduction

The world faces growing challenges related to environmental pollution, particularly water contamination, and the need for sustainable energy solutions. According to recent estimates, over 1.2 billion people lack access to sufficient drinking water, and increasing carbon emissions from fossil fuel use exacerbate global environmental concerns, leading to environmental issues that necessitate the search for an alternative sustainable energy supply.[1–5] Additionally, agricultural runoff containing harmful chemicals such as pesticides, organic dyes, and industrial waste further pollutes water bodies, causing significant risks to human welfare and ecosystems.[6–9] In response to these challenges, solar-light-driven photocatalysis has emerged as a promising, eco-friendly technology.[6] This process utilizes semiconductors to produce reactive oxygen species (ROS) such as superoxide ($^•O_2^-$), peroxide ($O_2^•$), and hydroxyl radicals ($^•OH$), which can degrade pollutants, reduce $CO_2$ into hydrocarbon fuels, and address various environmental issues.[10–13] These charge carriers facilitate the pro-

duction of ROSs, which are involved in the degradation of inorganic and organic pollutants, and the reduction of $CO_2$ to hydrocarbon fuels.[14–16] Research has extensively explored semiconductor-based heterogeneous photocatalysis driven by direct solar energy or other light sources using materials such as g-$C_3N_4$,[17–19] perovskites,[20] quantum dots,[21] $TiO_2$,[22] $Bi_2WO_6$,[23] $CuO$,[24] $ZnO$,[25] $CdS$,[26] $ZnS$[27] and $Fe_3O_4$.[28] However, photocatalytic applications face challenges such as large bandgaps, fast recombination of photogenerated charge carrier pairs, photocorrosion, limited solar energy application, and low recyclability, all of which restrict their photocatalytic performance.[29–31] Therefore, it is essential to develop innovative photocatalysts with inclusive applications.

Over the last several decades, there has been an extensive surge in attention to MOFs as encouraging photocatalysts attributed to their extensive surface area, elevated porosity, and adjustable structures, and they have emerged as promising microporous crystalline materials within the coordination polymer family.[32–34] MOFs consist of inorganic metal components linked by organic materials to create one-dimensional, two-dimensional, or three-dimensional micro- or nanoporous systems. With their unique structures and properties, MOFs have found applications across various fields, including photocatalysis, adsorption, clean energy generation, electronics, energy storage, and medical applications.[35–38] MOF-templated

*Centre for Nanoscience and Nanotechnology, Siksha 'O' Anusnadhan (Deemed to be University), Bhubaneswar, Odisha, 751030, India.
E-mail: kulamaniparida@soa.ac.in, paridakulamani@yahoo.com;
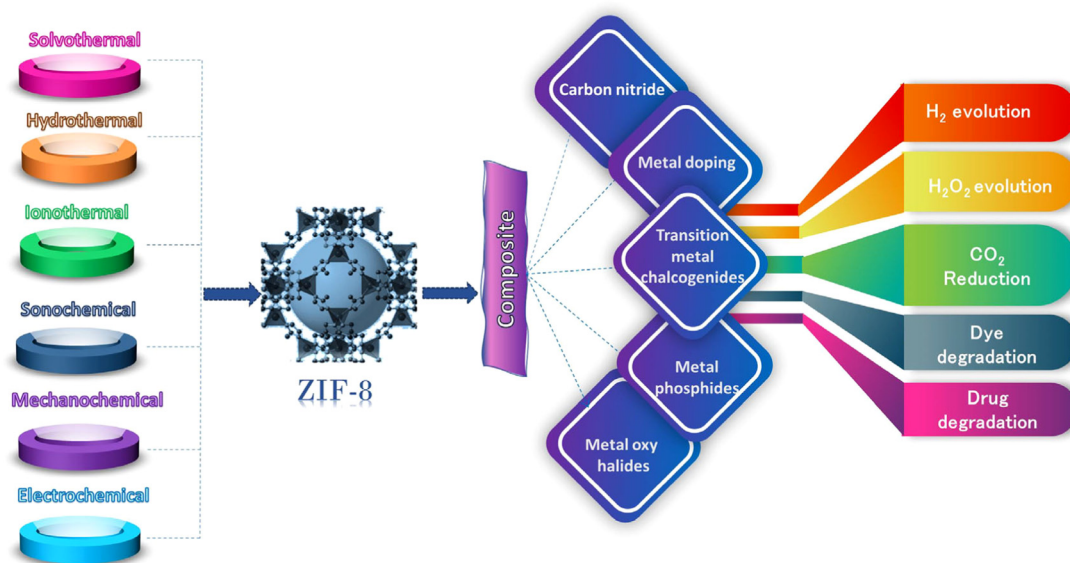Fax: +91-674-235064; Tel: +91-674-2351777*

**Fig. 1** Schematic representation of the overall contents of the review.

photocatalysts are particularly valued for their high surface area, which enhances active site exposure, mass transfer, and charge carrier transport.[39–41] Their tunable properties, superior adsorption capacity, flexible frameworks, and multi-functionality make MOFs highly promising as porous photocatalysts.[42,43] MOFs are characterized by their crystalline nature and exceptional porosity.[44] With impressive surface areas exceeding 6000 $m^2$ $g^{-1}$ and pore diameters ranging from 5 to 25 angstroms, MOFs exhibit nearly 90% of free volumes.[45] Additionally, their band gaps render them responsive to light, enabling them to utilize solar energy effectively.[46] Their size-able specific surface area facilitates an even and extensive dispersion of active species, benefiting the catalyst's performance.[47] Moreover, MOFs' elevated porosity enhances their ability to adsorb and absorb gases, and the pores can house active species, protecting them from deactivation due to agglomeration.[48]

By modifying synthesis conditions, various functional MOFs can be created due to their highly adaptable structures. ZIFs are attracting considerable attention because of their outstanding chemical and thermal resistance, maximum yield, modifiable micropore shapes and sizes, and flexible design and functionality.[49,50] One notable example of ZIFs is ZIF-8, renowned for its excellent chemical and thermal stability. ZIF-8 comprises Zn(II) ions and 2-methylimidazole ligands. Based on the Hard and Soft Acids and Bases (HSAB) theory, Zn(II) ions create robust coordination bonds with azolate ligands, resulting in the bond between Zn(II) and 2-methylimidazole being among the most stable coordination interactions.[51,52] ZIF-8 offers advantages such as an extensive surface area, adjustable pore sizes, active channels, flexible chemical structures, and intense hydrophobicity. ZIF-8's synergistic interaction between the $Zn^{2+}$ metal center and imidazolate linker provides abundant active sites for photocatalysis, surpassing

traditional semiconductors like $TiO_2$ and ZnO, which rely on fixed material structures.[53] The $Zn^{2+}$ center serves as a redox site, facilitating electron transfer, charge stabilization, and reduced recombination, while the organic linker enhances photocatalytic interactions *via* coordination bonds, π–π stacking, and charge transfer. This hybrid system enables broader light absorption, tunable band gaps, and higher reactivity compared with conventional materials. The porous, high-surface-area framework of ZIF-8 supports guest molecule encapsulation, doping, and multifunctional catalysis, enhancing catalytic efficiency. Its structural flexibility and selective interactions make it ideal for targeted photocatalytic applications like $CO_2$ reduction and pollutant degradation, while its stability under irradiation resists photodegradation, unlike $TiO_2$ or CdS.[54] Additionally, ZIF-8 can be prepared at RT with minimal expense. Nonetheless, it has certain limitations: (i) ZIF-8 often clumps together in water, leading to the growth of particle dimensions and resistance to transfer, which diminishes their adsorption capacity; (ii) extracting ZIF-8 nanomaterials from aqueous solutions is demanding, hindering their ability to be regenerated and reused; (iii) ZIF-8 has a limited response to visible light due to its broadband gap, which reduces its effectiveness under solar irradiation. Consequently, the application of ZIF-8 monomers is significantly limited.[55] To address these issues, photoactive molecules or semiconductors are combined with ZIF-8 to create ZIF-8-based binary or ternary photocatalysts. The formation of these novel multifunctional composites or hybrids is achieved by carefully combining ZIF-8 with functional materials. Unlike single-component photocatalysts, while rapid electron–hole recombination is common, thoughtfully engineered composite photocatalysts can leverage the combined advantages of each individual component while mitigating their drawbacks, leading to enhanced photocatalytic efficiency.[56] Various ZIF-8-

based composites, including oxides,[57] sulfides,[46] $C_3N_4$,[58] and metals,[48] have been developed to date. These hybrids have demonstrated outstanding photocatalytic performance compared with pristine ZIF-8.

This review article offers a comprehensive analysis of ZIF-8 and its hybrid materials, highlighting their dual role in energy generation and environmental remediation. Unlike existing studies that often focus on either adsorption or specific photocatalytic applications, this work uniquely integrates insights across both domains. It demonstrates how ZIF-8-based materials can address clean energy needs, such as hydrogen and hydrogen peroxide production, while simultaneously tackling pollutant degradation and wastewater treatment. This dual approach positions ZIF-8 as a versatile platform for sustainable energy solutions and environmental protection. By bridging these critical areas, the review presents a unified framework for designing multifunctional photocatalytic systems that meet global energy and environmental challenges, marking a significant contribution to the field. The urgency of this work is underscored by the increasing need for sustainable solutions to global challenges like energy shortages and water pollution, making this review a timely and valuable contribution to the field. So this review aims to fill these gaps by providing an integrative analysis of the dual functionality of ZIF-8-based materials in energy generation and environmental remediation. It systematically summarizes recent progress in ZIF-8's structural engineering, highlighting strategies such as doping with metals and composite formation with semiconductors to enhance photocatalytic efficiency. The review further delves into the mechanisms driving ZIF-8's photocatalytic activities, offering a holistic understanding of its role in addressing global challenges in sustainability. Here we have outlined various preparation techniques for ZIF-8 and ZIF-8-based hybrid synthesis in photocatalysis, offering theoretical guidance and promoting the development of ZIF-8-based photocatalysts and summarizing recent advances in ZIF-8 and their hybrids for energy and environmental applications, with a focus on synergistic effects that enhance the stability and photocatalytic activity of these materials. Lastly, it discusses the current challenges and future directions. Overall, this review not only establishes a foundational database for ZIF-8 MOFs and their photocatalytic properties but also provides strategic insights for designing and synthesizing ZIF-based MOFs with possible applications within the discipline of photocatalysis (Fig. 1).

## 2. Overview of ZIF-8 metal–organic framework

ZIFs are a subclass of MOFs that have garnered widespread attention because of their combination of zeolite and MOF properties, such as extensive surface area, crystallinity, microporosity, and notable chemical and thermal stability.[59,60] They are named for their zeolite-like structure, where the typical tetrahedral aluminum or silicon with bridging oxygen is replaced by zinc or silicon bridged by imidazolate. Both structures share a bond angle of 145°, as illustrated in Fig. 3a. Numerous ZIFs have been documented, typically featuring metal ions like cobalt or zinc connected through nitrogen to imidazolate linkers, forming adjustable nanopores.[61] These pores are created by a $CoN_4$ or $ZnN_4$ tetrahedral complex, which allows guest molecules to enter for applications in catalysis and gas storage and enable molecular-level differentiation for gas separation. Imidazole is part of the heterocyclic compound family, characterized by a 5-membered ring structure. Its chemical formula is $C_3N_2H_4$, consisting of 3 carbon atoms and 2 nitrogen atoms positioned at the 1st and 3rd locations in the ring (Fig. 3b). Due to the hydrogen atom's ability to link with either nitrogen atom, imidazole exists in two tautomeric states.[62] Also referred to as 1,3-azole, imidazole is a strongly polar compound that dissolves easily in water and displays amphoteric properties, meaning it can act as both an acid and a base.[63] In its solid form, imidazole is a white, colorless substance with a boiling point of 267.8 °C and a melting point of 88.9 °C.[64]

Compared with zeolites, ZIFs possess greater flexibility owing to their inorganic–organic framework and functionalized imidazolate linkers. This flexibility allows easier control over their structures and pore sizes, enabling greater ease in modifying their properties. ZIF-8, one of the most extensively researched ZIFs, consists of zinc tetrahedral clusters linked by 2-methyl imidazolate. It is synthesized using zinc salt and 2-methyl imidazole, forming a sodalite (SOD) type zeolite structure that takes the shape of a truncated octahedron.[59] These octahedrons interconnect to form a 3D framework, as shown in Fig. 3c. Initially synthesized by Yaghi *et al.* in 2006 through solvothermal methods, ZIF-8 and other ZIFs demonstrate significant chemical resistance in heated organic solvents, water, and alkaline aqueous solutions, a trait not observed in other MOFs (Fig. 3d).[45,59]

ZIF-8 possesses extremely high surface areas. In Yaghi's initial study, ZIF-8 demonstrated a Brunauer–Emmett–Teller (BET) surface area of 1630 m² g⁻¹, significantly exceeding any zeolite, providing abundant active sites that enhance the adsorption of reactant molecules like dyes, drugs, and water, thereby improving photocatalytic efficiency.[59,65,66]

Its microporous structure, with pore openings of 3.4 Å and pores with a diameter of 11.6 Å, is attributed to the methyl groups on the imidazolate linkers. As a result, pore sizes are roughly twice those of zeolites, while the apertures are analogous to the minimal molecular sieves, enabling selective adsorption and diffusion of target molecules, facilitating the trapping of reactants and intermediates to boost degradation and energy conversion processes.[59]

ZIF-8 is also thermally and chemically stable, enduring a wide range of temperatures and pH conditions, making it ideal for harsh photocatalytic environments, such as acidic or basic systems used in pollutant degradation.[67]

Although its wide bandgap (~5.1 eV) limits direct photocatalysis under visible light, ZIF-8 serves as an excellent support material for narrow-bandgap semiconductors, for facilitating

charge transfer when doping with metals (Cu, Ag) or combined with other photocatalytic materials like (TiO$_2$, Cu$_2$O, g-C$_3$N$_4$), improving light absorption and charge separation, and reducing the recombination of charge carriers.[65,66]

ZIF-8 is stable and insoluble in water and methanol, even in reflux conditions, and resists hydrolysis, which is uncommon among zinc-based MOFs. This exceptional stability is attributed to two factors: the strength of the bond between the imidazolate nitrogen and the metal ion, which is analogous to covalent solids.[68] The hydrophobic nature of ZIF-8 pores, which deters water molecules and prevents their attack on the MIm$_4$ (M = Zn) tetrahedral units, which contributes to ZIF-8's exceptional stability, is highly advantageous for various applications, allowing it to withstand harsh chemical and thermal environments.[69]

The structural tunability of ZIF-8, achieved through ligand modification or metal ion substitution, optimizes its electronic properties, surface chemistry, and light-harvesting abilities for targeted applications. Moreover, its metal center (Zn$^{2+}$) facilitates electron transfer, enhancing the generation of ROSs such as hydroxyl radicals and superoxide anions, crucial for photocatalytic oxidation.[70]

Finally, ZIF-8 acts as a stabilizer or protective layer for embedded semiconductors, reducing photocorrosion and ensuring long-term activity, particularly for sensitive materials like Cu$_2$O. These characteristics collectively make ZIF-8 a versatile and robust platform for photocatalytic applications in energy generation and environmental remediation (Fig. 2).[71]

# 3. Synthesis procedures

The synthesis strategies for creating ZIF-8 structures with desirable and valuable properties are influenced by various synthetic factors. The primary precursors for ZIF-8 fabrication are zinc metal and 2-methylimidazole. Several parameters need to be fine-tuned during the crystallization procedure, including the concentration of starting materials, temperature, solvent choice, and agitation rate. In this discussion, we explore several methods for synthesizing ZIF-8, including solvothermal, hydrothermal, ionothermal, sonochemical, mechanochemical, and electrochemical synthesis.

## 3.1 Solvothermal

In the pioneering work by Yaghi *et al.*, solvothermal synthesis was used to create twelve distinct ZIF crystals, designated as ZIF-1 to ZIF-12, which were successfully synthesized using a range of organic solvents, including methanol, *N,N*-dimethylformamide (DMF), *N*-methyl pyrrolidine (NMP) and *N,N*-diethylformamide (DEF).[59,72] To aid the formation, organic amines like pyridine and triethylamine (TEA) were introduced as deprotonating agents into the DMF or DEF solvent. The development and architecture of ZIF-8 feature large spherical cages called sodalite cages connected by six-ring windows.[73]

Methanol's versatility as a solvent in organic synthesis prompted various research groups to explore its use in ZIF synthesis, with additives such as high molecular weight, which was found to enhance ZIF-8 formation.[74] Chen *et al.* later achieved the synthesis of ZIF-8 (initially referred to as MAF-4) using methanol as the reaction medium. This involved a meticulous layering process where a methanol solution containing 2-methylimidazole was gradually coated onto an aqueous ammonia solution, including Zn(OH)$_2$, over the course of one month.[75] Following this, Venna *et al.* introduced an approach for synthesizing ZIF-8 *via* the solvothermal method, with methanol as the solvent. They initiated the process by stirring the mixture for 5 minutes at room temperature before transferring it into a Teflon-lined autoclave. Subsequently, the solution was heated for 5 hours at 150 °C under autogenous pressure. This approach, while still utilizing comparatively elevated temperatures, significantly reduced the time required for syn-
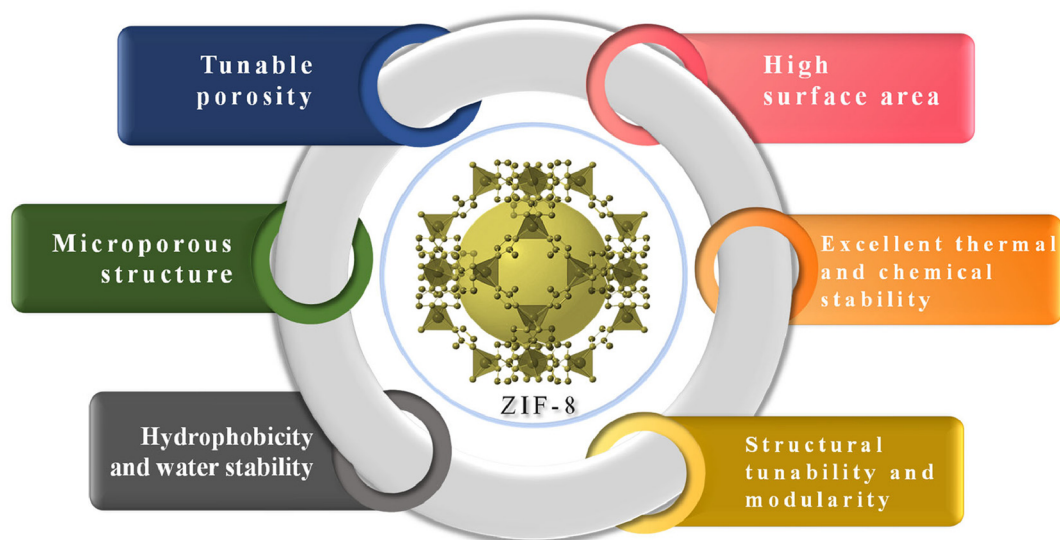


**Fig. 2** Schematic representation of various properties of ZIF-8.

thesis and benefited from the cost-effectiveness of methanol as a solvent. The structure of ZIF-8 crystals was also examined. The average crystal size of ZIF-8 was approximately 45 nm, determined using Scherrer's equation from the amplifying of the X-ray diffraction (XRD) peaks shown in Fig. 3e. TEM analysis confirmed the formation of ZIF-8, with diffraction rings matching XRD peaks and indicating a body-centered cubic arrangement with a unit cell dimension measuring 16.48. TEM images revealed sharp, hexagonal crystals around 55 nm, with lattice fringes corresponding to the (222) planes, captured with minimal TEM exposure to prevent crystal amorphization.[76] Further nanoscale ZIF-8 was synthesized using methanol by combining a solution of methanol containing Zn $(NO_3)_2$ and 2-methylimidazole under ambient conditions.[77]

To refine the synthesis process, Wiebcke *et al.* introduced sodium 1-methylimidazole/formate and *n*-butylamine as modulating ligands into methanol solutions, allowing for the regulation of ZIF-8 crystal size. This adjustment enabled the tuning of crystal sizes ranging from 10 to 65 nm for nanocrystals or approximately 1 mm for microcrystals. Through the utilization of *ex situ* scanning electron microscopy (SEM) and *in situ* energy dispersive X-ray diffraction (EDXRD), we have demonstrated that the solvothermal crystallization of ZIF-8, modulated by sodium formate, proceeds rapidly, resulting in the formation of large, high-quality single crystals within a brief timeframe (<4 hours).[83,84] Alternative alcohols like isopropyl alcohol and ethanol also demonstrated effectiveness in this context. However, concerns over the costly, toxic, and flam-
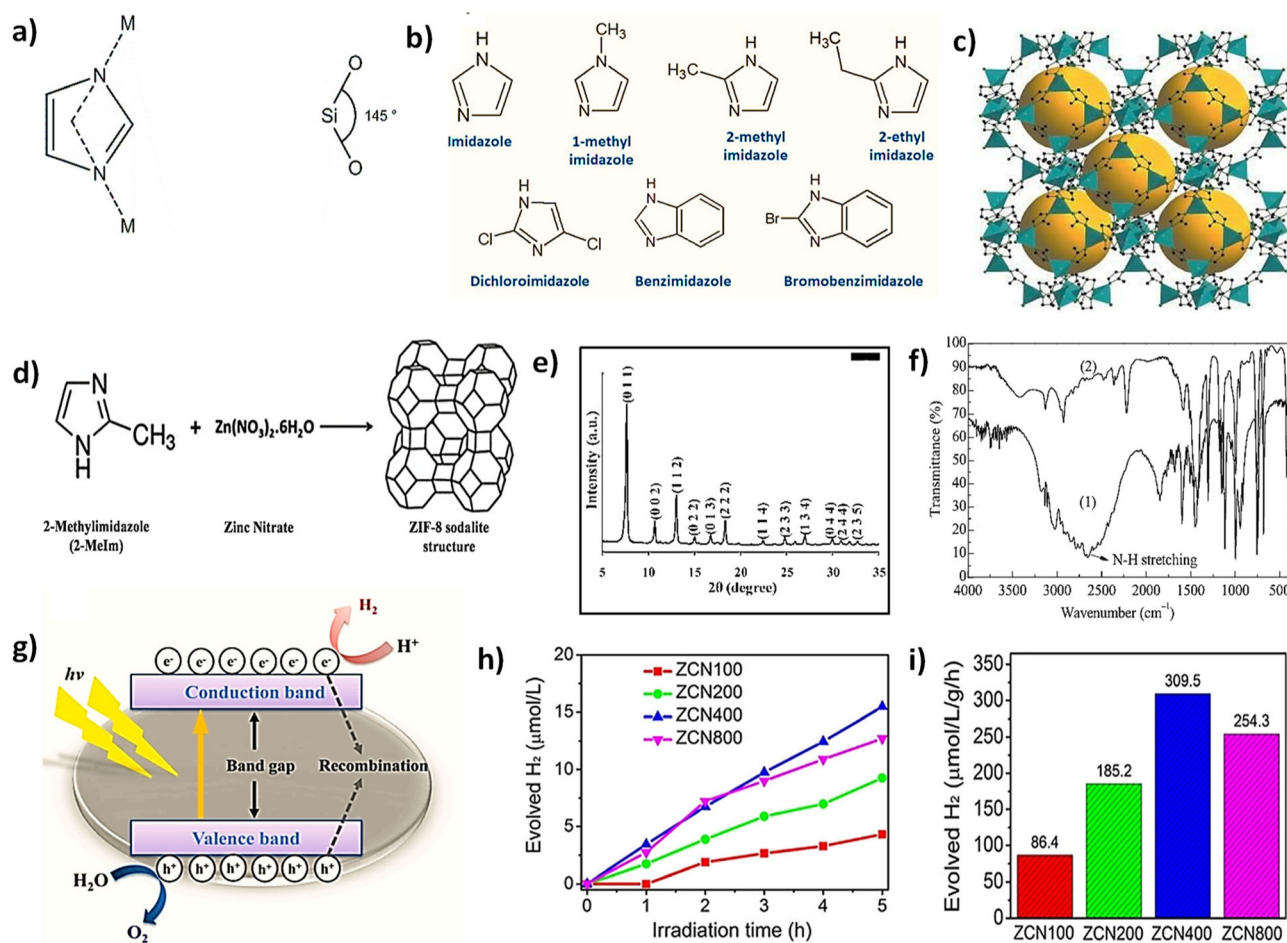


**Fig. 3** (a) The bridging angle in both ZIFs and zeolites is 145° [reproduced from ref. 78 with the permission from The University of Liverpool]. (b) Imidazole and certain derivatives of it are utilized as linkers [reproduced from ref. 79 with the permission from Elsevier, copyright 2023]. (c) The structure of ZIF-8, with yellow spheres representing the pore volume [reproduced from ref. 78 with the permission from The University of Liverpool]. (d) Sodalite structure of ZIF-8 formed from zinc metal and 2-methylimidazole [reproduced from ref. 45 with the permission from Elsevier, copyright 2017]. (e) XRD pattern of ZIF-8 crystals used for membrane fabrication [reproduced from ref. 76 with the permission from American Chemical Society, copyright 2010]. (f) FTIR spectra of 2-methylimidazole (1) and ZIF-8 sample (ILs-R1) (2) synthesized *via* the ionothermal method in [emim]Br [reproduced from ref. 80 with the permission from Elsevier, copyright 2015]. (g) Photocatalytic hydrogen generation through water splitting [reproduced from ref. 81 with the permission from Elsevier, copyright 2020]. (h) Solar-powered photocatalytic hydrogen generation performance, including hydrogen production rates (i), for various ZIF-8/modified g-$C_3N_4$ nanocomposites ZCN X [reproduced from ref. 82 with the permission from Elsevier copyright 2018].

mable nature of organic solvents prompted a shift towards hydrothermal synthesis methods during this period.[85]

### 3.2 Hydrothermal

Researchers have opted for water, the most economical solvent available, in their endeavors, wherein a solution of zinc(II) nitrate is immersed in an excess amount of 2-methyl-imidazole (Hmim/Zn = 70).[86] This approach aligns with the growing trend of adopting greener and simpler methods, reducing reliance on toxic organic solvents. Additionally, water-based processes for ZIF production have been optimized with additives. Under ambient temperature, ZIF-8 nanoparticles can be synthesized *via* the hydrothermal method, which involves three main stages: (a) dissolving zinc sources in demineralized water, (b) dissolving organic ligands in demineralized water, and (c) combining both the solutions to initiate the reaction and generate ZIF-8 particles.[87] Ding and his co-workers reported that the hierarchically structured ZIF assembled through the hydrothermal technique exhibited a surface area of 304 m$^2$ g$^{-1}$, with dimensions of several micrometers in length, 1–2 micrometers in width, and around 300 nm in thickness.[88] Song *et al.* capitalized on the benefits of the hydrothermal process and the unique properties of ZIF-8. The XRD pattern indicates that the product possesses a dense diamond (Zn) structure. As depicted in the SEM image, the product exhibits a characteristic plate-like morphology, with dimensions typically ranging from 3 to 5 μm. It is plausible to infer that an excess of water diminishes the overall solution's basicity, thereby retarding the deprotonation rate of Hmim.[85]

Butova *et al.* (2017) demonstrated a streamlined approach in utilizing triethylamine (TEA) to synthesize a ZIF-8 catalyst in a single phase with remarkable properties: a large specific surface area of 1340 m$^2$ g$^{-1}$, and excellent thermal stability up to 470 °C in N$_2$ and 400 °C in air, all achieved in water without the need for organic solvents.[89] In a separate study, Oozeerally *et al.*, in 2019, compared two synthesis methods for ZIF-8: hydrothermal synthesis at 140 °C and room temperature synthesis. The hydrothermal method yielded a compound with an exceptional specific surface area of 1967 m$^2$ g$^{-1}$, rendering it highly applicable.[90] ZIFs synthesized *via* the hydrothermal method typically exhibit a particle size of about 100 nm, while those made using the solvothermal approach have a particle size closer to 30 nm. Several composites and heterojunctions incorporating ZIF-8, such as Zn$_2$SnO$_4$/ZIF-8,[91] ZIF-8/NiFe$_2$O$_4$,[92] and ZIF-8@TiO$_2$ core–shell micron composites,[93] have been effectively fabricated using the hydrothermal process.

### 3.3 Ionothermal

A novel synthesis approach known as ionothermal synthesis has emerged for the production of ZIF materials.[94,95] Cooper *et al.* suggested an alternative solvothermal method for preparing ZIFs, utilizing an ionic liquid as the medium.[96] This novel method, known as the ionothermal technique, is gaining significant interest among researchers working with various ZIFs. In ionothermal synthesis, the ionic liquid acts as a salt capable of melting at temperatures between 150 °C and

200 °C, the range typically used for synthesizing zeolites.[94] This method utilizes environmentally friendly solvents such as eutectic mixtures and ionic liquids, which offer several advantages and exhibit fascinating properties that make them exceptional solvents. These properties include stability at elevated temperatures, high solubility for both non-polar and polar inorganic and organic compounds, low melting point, and suitable viscosity, along with the advantages of having minimal vapor pressure and being non-flammable. Additionally, a significant advantage of ionic liquids is their ability to be recycled and reused, contributing to sustainable practices.

Morris and his team were the first to recognize the feasibility of employing ionic liquids in the synthesis of ZIFs. They documented the generation of four ZIFs, with structures either known or novel, under ionothermal parameters utilizing the ionic liquid 1-ethyl-3-methylimidazolium bis[(trifluoromethyl)sulfonyl] imide.[97] Martins and coworkers introduced an ionic liquid synthesis approach utilizing the commercially available IL 1-ethyl-3-methylimidazolium bis(trifluoromethylsulfonyl)imide.[97] This synthesis methodology has garnered considerable interest among researchers due to its adaptability in an open system.

Wang and colleagues detailed the production of various ZIFs, notably ZIF-8, through the ionothermal method. The XRD spectra for the ZIF-8 and ZIF-67 samples corresponded closely with the simulated patterns derived from the sod-type single-crystal data. The FTIR spectrum of the ZIF-8 sample shows that the vibrational frequency for the N–H bond of 2-MIm at 3335–2500 and 1820 cm$^{-1}$ has vanished, indicating complete deprotonation of 2-MIm upon coordination with Zn (Fig. 3f). This finding indicates that the samples produced by both rapid and controlled cooling methods were pure-phase sodalite-type ZIFs. The SEM micrographs of ZIF-8 and ZIF-67 samples created through rapid cooling had an aggregated spherical shape with average particle sizes of 0.5 μm and 0.35 μm, respectively. Conversely, samples cooled through programmed cooling displayed truncated rhombic dodecahedral shapes, with dimensions of 50 μm and 5 μm for ZIF-8 and ZIF-67, respectively. These findings underscored that samples cooled *via* programmed methods yielded larger and more uniform structures compared with those cooled rapidly.[80]

### 3.4 Sonochemical

The sonochemical method involves using ultrasound waves to facilitate chemical reactions, leading to reduced reaction times compared with solvothermal synthesis. It can also be called the sono-crystallization process. This synthesis offers an alternative approach to producing ZIFs, complementing conventional oven heating methods. This method not only facilitates nucleation but also ensures homogeneous dispersion of nucleation.[98] The sonochemical method involves generating and collapsing bubbles in solutions, known as acoustic cavitation, which generates high pressures, temperatures, and rapid cooling and heating rates.[99]

Research by Seoane *et al.* indicates that under ultrasound radiation at a frequency of 47 kHz and a power of 110 W, pure ZIF-8 frameworks were formed at very low temperatures

(45–60 °C) and briefer durations (6–9 hours) compared with traditional solvothermal synthesis methods. By incorporating a synthetic activator and enhancing the substrate concentration ($Zn^{2+}$ : DMF = 1 : 9.3), an 85% yield was achieved. Consequently, the sonochemical method proves more favorable for rapidly synthesizing smaller-sized ZIF-8 particles. SEM images of the ZIFs were prepared through sonocrystallization. By analyzing these SEM images, cumulative crystal size distributions were derived. Moreover, these crystals were observed to be smaller and exhibited a narrower particle size distribution compared with conventionally synthesized materials.[100]

Recent work by Cho and his colleagues demonstrated the successful synthesis of abundant amounts of ZIF-8 employing a direct ultrasonic method in dimethylformamide in the midst of NaOH and triethylamine as a modulating agent. It exhibited comparable physiochemical properties, thermal stability, and chemical stability to traditional synthesized ZIF-8 but with a significantly reduced reaction time of 24 hours.[101] Furthermore, they achieved scale-up to a 1-liter synthesis of ZIF-8 through this sonochemical synthesis process, showing potential for industrial applications.

### 3.5 Mechanochemical

Mechanochemistry, as an environmentally friendly and efficient approach, has exhibited remarkable potential, and it involves ball milling for the fabrication of ZIFs.[102] By eliminating the need for solvents and salts during the synthesis method, the mechanochemical synthesis method can significantly decrease environmental pollution and minimize the incorporation of impurities within the crystal lattice. In 2006, the initial step towards obtaining nonporous $Zn(IM)_2$ was achieved through manual milling of ZnO with a substantial excess of IM.[103,104] Adams *et al.* demonstrated the generation of nonporous $Zn(IM)_2$ products through a two-step mechanochemical process initiated from $ZnCl_2$.[104,105]

Recognizing the constraints associated with oxide-based precursors in direct grinding for ZIF synthesis, Friščić *et al.* introduced advanced mechanochemical approaches known as liquid-assisted grinding (LAG) and ion- and liquid-assisted grinding (ILAG). These techniques allowed the formation of ZIFs from a balanced 1 : 2 molar ratio of ZnO and various ligands, including imidazole, 2-ethylimidazole, and 2-methylimidazole, at ambient temperature.[106,107] It was observed that adding a small-volume liquid phase enhanced molecular mobility, while salt additives accelerated ZIF formation.[108] Moreover, the topology of the resulting ZIFs could be adjusted by varying the milling liquids (such as ethanol, DMF, and DEF) and salt enhancers (like $NH_4NO_3$, $NH_4CH_3SO_3$, and $(NH_4)_2SO_4$). Friščić *et al.* also monitored the ball mill grinding process, the synthesis of intermediates, and the transition of ZIF topologies through *in situ* high-energy synchrotron X-ray diffraction.[109]

Lately, Tanaka and co-authors showcased a completely solvent-free mechanical transformation of ZnO to ZIF-8 free from any additional substances. They accomplished this by adding nano-sized ZnO powders (averaging 24 nm in particle size) along with MIm into a ball mill operating at 100 rpm.[110]

It was observed that larger nanoparticles retained untransformed ZnO, whereas smaller nanoparticles did not, indicating that nano-sized ZnO particles were more prone to converting into ZIF-8. The suggested mechanism involves the breaking down of nanoparticle agglomerates into smaller pieces, followed by the formation of complexes *via* the reaction between ZnO and MIm. The resulting ZIF-8 agglomerates into nanoparticles, which subsequently coat the ZnO. Besides crystalline ZIFs, Cheetham and his team demonstrated the synthesis of amorphous ZIFs through ball milling. Through grinding, various amorphous ZIF products can be synthesized.

### 3.6 Electrochemical

For more than a decade, researchers have employed the electrochemical synthesis method to produce MOFs.[111] This method is categorized into cathode synthesis and anode synthesis based on the underlying reaction mechanisms. In the solution, anode synthesis involves the dissolution of metals at the anode, forming metal ions that subsequently self-assemble with organic linkers. On the other hand, cathode synthesis utilizes oxoacidates such as $NO_3^-$ or $ClO_4^-$ to create an alkaline gradient near the cathode. This gradient aids in the deprotonation of organic linkers, facilitating their self-assembly with incorporated metal ions.[112]

Researchers have increasingly turned to electrochemical synthesis methods to produce ZIF-8 crystals, drawn by their numerous advantages: low energy requirements, mild operational conditions, rapid kinetics, significant yields, and simplicity of operation and equipment.[113] Martinez Joaristi and co-authors utilized an anode synthesis method to fabricate ZIF-8 using solvents such as water, ethanol, methanol, and DMF. Notably, ZIF-8 synthesis exhibited flexibility in electrolyte choice ($Na_2SO_4$, KCl, or $KNO_3$) and achieved reduced synthesis durations (<20 min).[114]

Worrall *et al.* successfully synthesized 5 ZIF coatings using the anodic method, incorporating 2 metals, zinc and cobalt, along with 4 different linkers: imidazole (IM), benzimidazole (bIM), 2-methylimidazole (mIM), and 2-ethylimidazole (eIM). PXRD confirmed the composition of the coatings which verified the synthesis of ZIF-8, that shares the stable SOD structure, when zinc and mIM were used as precursors. SEM was employed to analyze the quality and morphology of the ZIF coatings, and the SEM images suggested tiny crystals with unclear morphology constituting the coating. However, upon in-depth examination, the expected morphology of rhombic dodecahedral characteristic of ZIF-8 crystals became evident.[115]

The research group of Li proposed a three-electrode setup for an easy and adaptable electrochemical approach to synthesize ZIF-8, ZIF-67, as well as hybrid ZIF-67/ZIF-8 films. These films displayed coherent and consistent properties when deposited on conductive substrates (such as FTO, carbon cloth, and Ni foam) and nanostructured materials in just seconds at standard ambient temperature. An especially significant benefit was the ability to precisely regulate film thickness at the micron scale by adjusting the electrosynthesis time.[116]

The synthesis of ZIF-8 materials demonstrates the versatility and adaptability of different methods, each offering unique benefits and limitations. From traditional solvothermal and hydrothermal approaches to more novel ionothermal, sonochemical, mechanochemical, and electrochemical methods, advancements have been made to optimize crystal size, morphology, and yield while promoting environmental sustainability and scalability. Each method fine-tunes parameters such as solvents, temperatures, and additives, showcasing the diverse strategies available for ZIF-8 production, making it a promising material across various applications. Table 1 summarizes the advantages and disadvantages of the abovementioned synthetic procedures.[99,117–123]
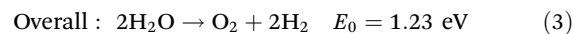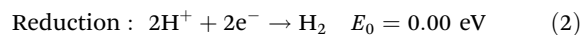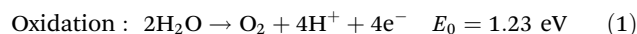
# 4. Photocatalytic applications

ZIF-8 demonstrates photocatalytic potential due to its extensive surface area, high porosity, and exceptional chemical stability, which enhance the adsorption and interaction of reactant species. Although its direct light-harvesting ability is constrained by a broad bandgap, the incorporation of ZIF-8 with photoactive semiconductors augments its photocatalytic efficacy by promoting superior charge separation, efficient electron transport, and prolonged carrier lifetimes, thus driving enhanced photocatalytic processes.

## 4.1 H$_2$ evolution

Photocatalytic H$_2$ production from water is seen as a prominent solution to the global energy scarcity.[124,125] This process involves three key stages: (1) photons with energy exceeding the bandgap excite electrons in the valence band (VB) to the conduction band (CB), resulting holes in the VB; (2) the resulting charge carriers separate and emigrate to the material's surface; (3) electrons in the CB reduce adsorbed H$^+$ to H$_2$, while holes in the VB oxidize water into oxygen. These steps are crucial for the redox reactions required for H$_2$ production.[126]

$$\text{Oxidation}: 2H_2O \rightarrow O_2 + 4H^+ + 4e^- \quad E_0 = 1.23 \text{ eV} \quad (1)$$

$$\text{Reduction}: 2H^+ + 2e^- \rightarrow H_2 \quad E_0 = 0.00 \text{ eV} \quad (2)$$

$$\text{Overall}: 2H_2O \rightarrow O_2 + 2H_2 \quad E_0 = 1.23 \text{ eV} \quad (3)$$

For the H$_2$ evolution reaction (HER) to occur, the CB energy level must be lower than 0 V ($E(H^+/H_2)$) under the normal hydrogen electrode (NHE). Additionally, the VB energy level must be higher than 1.23 V ($E(O_2/H_2O)$) for the water oxidation reaction to proceed (Fig. 3g).[81]

The development of numerous photocatalysts has gradually made photocatalytic hydrogen production an ideal and feasible technology. Among them, g-C$_3$N$_4$ has garnered significant attention due to its appropriate energy band (2.8 eV), stable structure, cost-effectiveness, and easy availability. Since 2009, g-C$_3$N$_4$ has been extensively utilized in photocatalytic H$_2$ generation. Thus, Tian and his team effectively incorporated ZIF-8 nanoparticles onto a modified rod-like g-C$_3$N$_4$ structure. The ZIF-8 nanoparticles display a sharply defined polyhedral crystal shape around 200 nm in average size, while the modified g-C$_3$N$_4$ materials form rod-like structures with irregular surface pores. This ZIF-8/g-C$_3$N$_4$ photocatalyst was used for H$_2$ evolution via solar-driven water splitting. Relative to pristine ZIF-8, the ZIF-8/g-C$_3$N$_4$ hybrid photocatalysts demonstrated a marked increase in hydrogen generation activity when exposed to light. Additionally, they investigated the impact of varying amounts of g-C$_3$N$_4$ on the photocatalytic efficiency of the ZIF-8/g-C$_3$N$_4$ hybrid, finding that 400 mg of g-C$_3$N$_4$ generated the highest H$_2$ production rate of 309.5 μmol L$^{-1}$ g$^{-1}$ h$^{-1}$ (Fig. 3h and i). This improved efficiency was supplied to the combined effects of the hybrid, which promoted excellent charge separation and light absorption.[82]

**Table 1** Comparative advantages and disadvantages of various synthesis methods

| Methods | Advantages | Disadvantages |
|---|---|---|
| Solvothermal | • Readily obtained single crystals<br>• Allows controlled tuning of particle morphology | • Requires soluble precursor reagents<br>• Large amounts of solvent waste generated<br>• Potentially hazardous handling of corrosive/explosive metal salts (chlorides, nitrates) in the presence of organic liquids |
| Hydrothermal | • Simple, easy and low-cost synthesis method<br>• Production of high quality 1D nanostructures<br>• The morphology is controlled by synthesis parameters | • The reaction takes a long time for high quality crystals<br>• Produces relatively large particle sizes, limiting surface area |
| Ionothermal | • Eliminates the need for toxic organic solvents by using ionic liquids | • High cost of ionic liquids limits large-scale application |
| Sonochemical | • Rapid synthesis, significantly reducing reaction time<br>• Produces smaller particles with narrow size distributions | • High-energy ultrasound equipment is necessary<br>• Limited scalability for large-scale production |
| Mechanochemical | • Solvent-free, eco-friendly, and low-cost synthesis<br>• Rapid and energy-efficient process | • Limited control over morphology and size of particles<br>• Not suitable for producing large quantities with uniform characteristics |
| Electrochemical | • High yield<br>• Less time required, morphology can be controlled through the control of synthesis parameters such as time, temperature etc. | • Unsuitable for large-scale production |

Nitrogen (N) vacancies on the interface of g-C$_3$N$_4$ create strong electronegativity, resulting in hydrogen adsorption and microbubble formation that obstructs reactions. In high-salinity seawater, charged ions occupy these N vacancies, competing with hydrogen protons for photogenerated electrons and further hindering hydrogen generation. For this, Xing et al. revealed that incorporating ZIF-8 into g-C$_3$N$_4$ eliminated the nitrogen-induced vacancies, enhancing hydrogen generation through photocatalytic seawater splitting. TEM images revealed numerous pores, about 32 nm in diameter, within the sheet structure of ZCNQ40. Nitrogen doping enhanced light absorption in all samples, leading to a decreased band gap. As shown in Fig. 4a, by DRS curves, the band gap of ZCNQ40 reduced from 2.66 eV to 2.58 eV, and the Mott–Schottky arcs of pristine g-C$_3$N$_4$ and ZCNQ40 both showed an ascending line, confirming their n-type semiconductor nature. The band alignment potential of ZCNQ40 shifted negatively by 0.09 V, from

−1.33 V for pure g-C$_3$N$_4$ to −1.42 V (vs. SCE), indicating a shift to lower energy in the conduction band potential. The composite containing 40 mg of ZIF-8 (ZCNQ40) produced the most H$_2$ in seawater, reaching 116.95 μmol L$^{-1}$ g$^{-1}$ h$^{-1}$, and in distilled water, achieving 218.4 μmol L$^{-1}$ g$^{-1}$ h$^{-1}$, with these rates being 5.6 times and 3.1 times higher, respectively, compared with those achieved with pure g-C$_3$N$_4$.[127] Suda et al. (2020)[128] developed an innovative hybrid Z-scheme photoactive catalyst by integrating copper-doped ZIF-8 with g-C$_3$N$_4$ for hydrogen production. The inclusion of g-C$_3$N$_4$ notably boosted the H$_2$ production rate from 32.2 μmol L$^{-1}$ g$^{-1}$ h$^{-1}$ to 213.3 μmol L$^{-1}$ g$^{-1}$ h$^{-1}$. This enhancement was due to the creation of a Z-scheme charge carrier separation mechanism resulting from the combination of copper-ZIF-8 with g-C$_3$N$_4$. Additionally, g-C$_3$N$_4$ optimized the absorption in the 480 nm range, which ZIF-8 alone could not capture.[128] Chang et al. developed a nitrogen-doped carbon (C-ZIF) decorated g-C$_3$N$_4$ hetero-
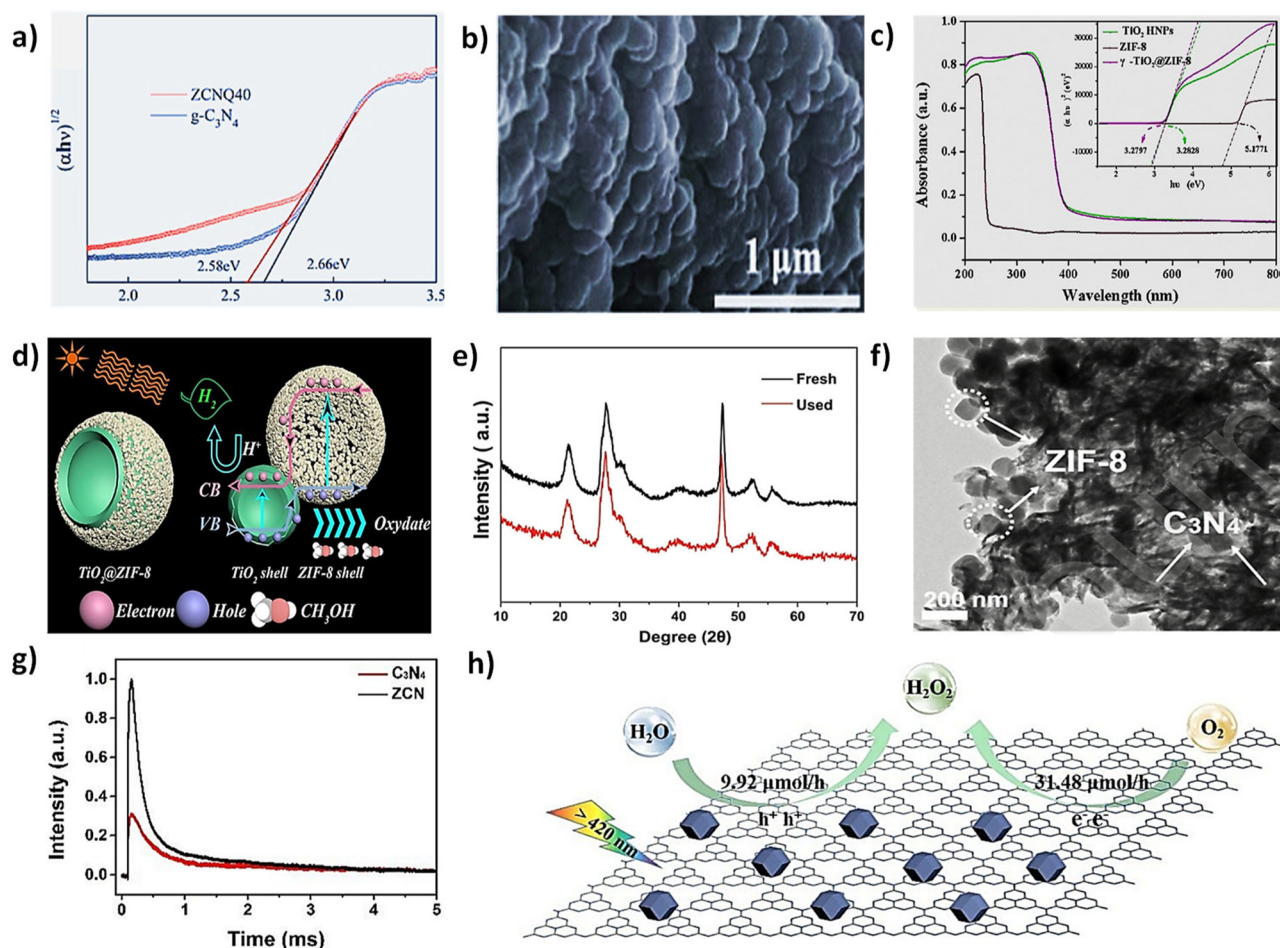


Fig. 4 (a) DRS spectra of g-C$_3$N$_4$ and ZCNQx [reproduced from ref. 127 with the permission from Elsevier, copyright 2021]. (b) SEM images of 10-C-ZIF@g-C$_3$N$_4$ [reproduced from ref. 129 with the permission from The Royal Society of Chemistry, copyright 2020]. (c) UV-Vis absorption spectra of TiO$_2$ HNPs, ZIF-8, and γ-TiO$_2$@ZIF-8; fitted curves of the Tauc plot (inset). (d) The hydrogen evolution reaction mechanism of TiO$_2$@ZIF-8 under simulated solar light irradiation [reproduced from ref. 130 with the permission of copyright 2015]. (e) XRD patterns of ZnS/ZIS-20 before and after repeated photocatalytic hydrogen production [reproduced from ref. 86 with the permission from The Royal Society of Chemistry, copyright 2020]. (f) TEM morphology of ZCN catalyst. (g) TPV of C$_3$N$_4$ (red line) and ZCN (black line). (h) The mechanism diagram for photocatalytic water splitting to produce H$_2$O$_2$ using ZCN [reproduced from ref. 131 with the permission from Elsevier copyright 2020].

structure through thermal treatment. This C-ZIF@g-C$_3$N$_4$ heterostructure, with an optimal ratio of C-ZIF and g-C$_3$N$_4$, displayed outstanding photocatalytic performance in H$_2$ generation compared with pure g-C$_3$N$_4$. The SEM images show that the C-ZIF maintains a rhombic dodecahedral structure with roughened surfaces after annealing and cleaning and is well-integrated with g-C$_3$N$_4$, forming a heterostructure with intense interfacial contact (Fig. 4b). The composite demonstrates outstanding H$_2$ evolution activity, achieving 1238 μmol g$^{-1}$ h$^{-1}$, which is 1.95 times greater than pure g-C$_3$N$_4$ and 1.57 times greater than 10-C-ZIF + g-C$_3$N$_4$. The increased results were attributed to effective charge transfer at the C-ZIF@g-C$_3$N$_4$ interface, which significantly restrained the recombination of photoexcited electron–hole pairs, thereby enhancing photocatalytic efficiency.[129]

Nanomaterials based on carbon, including carbon nanotubes, graphene, and graphitic PAN, can greatly enhance electron–hole separation in g-C$_3$N$_4$ through the formation of carbon/g-C$_3$N$_4$ composites, thereby boosting photocatalytic activity and serving as efficient HER catalysts. Inspired by this idea, He *et al.* developed C-ZIF-8/g-C$_3$N$_4$, derived from ZIF-8 carbon. Their study on photocatalytic H$_2$ evolution revealed that pure g-C$_3$N$_4$ produced hydrogen at a slow rate of 0.9 μmol L$^{-1}$ g$^{-1}$ h$^{-1}$, attributed to its inert surface for HER. The composite displays an IV-type isotherm, which suggests the presence of mesopores. As the carbon-ZIF content increases in the C-ZIF/g-C$_3$N$_4$ composites, the PL intensity significantly decreases, suggesting enhanced electron–hole separation due to the movement of photoexcited electrons from g-C$_3$N$_4$ to C-ZIF, which acts as an efficient electron receptor. Time-resolved fluorescence decay spectroscopy was used to determine the charge carrier lifetimes of g-C$_3$N$_4$ and the 1 wt% C-ZIF/g-C$_3$N$_4$ composite, both of which exhibited an exponential decay in their charge carrier lifetimes. The short lifetime increases from 1.27 ns in g-C$_3$N$_4$ to 2.39 ns in the composite, while the long lifetime extends from 9.33 ns to 13.93 ns. This increase in charge carrier lifetimes, due to the addition of C-ZIF, enhances photocatalytic efficiency. Remarkably, the inclusion of C-ZIF to g-C$_3$N$_4$ led to a notable increase in the photocatalytic hydrogen generation performance of the composite, reaching 32.6 μmol L$^{-1}$ g$^{-1}$ h$^{-1}$. This rate is 2.8 times greater than that of Pt/g-C$_3$N$_4$ and 36.2 times greater than pristine g-C$_3$N$_4$, indicating enhanced charge separation.[132]

Loading a photosensitizer like AgBr enhances the visible light response in materials. Upon decomposition, Ag$^+$ ions create a hybrid heterostructure that improves charge transfer and, due to their unique SPR effect, significantly boosts light absorption. Recently, to study this, Dai and colleagues successfully developed a three-component photocatalyst comprising Ag–AgBr/ZIF-8/g-C$_3$N$_4$ utilizing an ionic liquid-assisted *in situ* growth method. The HRTEM analysis of A(1.1)/g/Z(13) revealed a lattice spacing of 0.282 nm, associated with the (200) plane of AgBr, and the SAED pattern verified its crystalline structure. This newly formed system demonstrated significantly enhanced photocatalytic efficiency for hydrogen generation compared with ZIF-8, AgBr and g-C$_3$N$_4$. The enhancement was

largely due to the role of Ag$^+$, which served as a linking bridge, facilitating the creation of multiple electronic transmission pathways. XRD spectra confirmed Ag$^+$ within the composite, while AgBr increased the photocurrent density and acted as a photosensitizer. The AgBr/g-C$_3$N$_4$ and AgBr/ZIF-8 composites demonstrate higher photocurrent densities compared with their individual components. The A(1.1)/g/Z(6.5) composite achieves the maximum density, highlighting it as the optimal ratio. AgBr enhanced light absorption and formed a p–n heterojunction with g-C$_3$N$_4$, suppressing exciton recombination. The composite achieved a H$_2$ generation rate of 2058 μmol L$^{-1}$ g$^{-1}$ h$^{-1}$, which was 49 times more than that of unmodified g-C$_3$N$_4$ alone, maintaining 91% efficiency after 5 cycles.[133]

Transition metal chalcogenides, with their layered structure, direct band gap, and high absorption coefficient, are promising for hydrogen production.[134] For example, TiO$_2$ is highly effective in photocatalytic applications owing to its suitable band gap (~3.2 eV), strong oxidative power, high chemical stability, non-toxicity, cost-effectiveness, and photostability, ensuring its widespread use in solar energy applications. In 2019, Zhang and co-authors fabricated TiO$_2$@ZIF-8 by coordinative incorporation, employing TiO$_2$ hollow nanospheres (HNPs) coated with ZIF-8 through a sonochemical technique, and significantly enhanced HER under solar irradiation. The process involved a two-step approach: first modifying TiO$_2$'s surface to increase its area, followed by hybridizing it, the composite achieved a hydrogen production rate 3.5 times greater than pristine TiO$_2$ HNPs, with a quantum efficiency of up to 50.89% and notable stability. Optoelectronic measurements and photoluminescence indicated that ZIF-8's porous structure and effective charge separation improved the photocatalytic activity. The band gaps for ZIF-8, γ-TiO$_2$@ZIF-8, and TiO$_2$ HNPs were 5.18 eV, 3.28 eV, and 3.28 eV, respectively (Fig. 4c). The reduction in the $E_g$ values of the samples contributed to improved photocatalytic efficiency. The conduction band edges were −0.31 eV for TiO$_2$ and −4.73 eV for ZIF-8. Under artificial sunlight with methanol as the sacrificial reagent, bare ZIF-8 showed no H$_2$ evolution, while TiO$_2$ HNPs had an HER of 74.6 μmol g$^{-1}$ h$^{-1}$, limited by low surface area and fast charge carrier recombination. A physical mixture of ZIF-8 and TiO$_2$ HNPs displayed a reduced rate of 4.63 μmol g$^{-1}$ h$^{-1}$. However, the γ-TiO$_2$@ZIF-8 composite significantly enhanced the HER to 254.2 μmol g$^{-1}$ h$^{-1}$, 3.4 times greater than the pristine TiO$_2$ HNPs. The α-and β-TiO$_2$@ZIF-8 composites also improved the HER, to 186.1 μmol g$^{-1}$ h$^{-1}$ and 105.0 μmol g$^{-1}$ h$^{-1}$, respectively. The proposed mechanism for photocatalytic H$_2$ evolution is presented in Fig. 4d. Five successive photocatalytic tests were conducted under simulated sunlight, and the amount of H$_2$ produced consistently enhanced with irradiation time during every cycle. The system exhibited excellent stability over a prolonged period of 30 hours, with the hydrogen evolution rate in the fifth cycle.[130]

Bulk MoS$_2$, with a 1.2 eV band gap, is generally unsuitable as a photocatalyst due to its insufficient oxidation and reduction capabilities. However, exfoliated MoS$_2$ shows a direct band gap ranging from 1.89 to 3.96 eV as a result of

quantum confinement effects, enhancing its photocatalytic potential. For example, Ren and associates exfoliated $MoS_2$@ZIF-8 hybrid for the HER through sonication, showing improved absorption of light and hydrogen evolution reaction efficiency in comparison with pristine ZIF-8. The exfoliated photocatalyst revealed an absorption edge at 415 nm, suggesting an appropriate band structure for HER applications. The $MoS_2$@ZIF-8 composite had a measured band gap of 3.41 eV, which is shorter than the 5.15 eV band gap of pure ZIF-8. This composite structure obtained an $H_2$ generation rate of 68.4 $\mu$mol $L^{-1}$ $g^{-1}$ $h^{-1}$. The activity of MZ was analyzed by measuring hydrogen generation under using a Xe lamp. The $H_2$ generation rate for ZIF-8 was 0.01 $\mu$mol $h^{-1}$ $g^{-1}$, and bulk $MoS_2$ showed no activity. In contrast, the exfoliated $MoS_2$ (EM) in the MZ composite significantly enhanced the average $H_2$ evolution rate to 29.9 $\mu$mol $h^{-1}$ $g^{-1}$.[135]

ZIF-8 has been extensively utilized in the development of core–shell or core–shell-like catalysts. Zeng and co-authors created a novel core–shell structure, with ZIF-8 forming the shell and CdS NPs as the core. Initially, CdS nanoparticles were solidified using PVP and formed ZIF-8 shells on the CdS cores. Despite the limited hydrogen production rate of the resulting samples, the core–shell CdS@ZIF-8 structures exhibited enhanced specificity for hydrogen synthesis compared with pristine CdS NPs. The photocatalytic breakdown of formic acid was carried out to examine the harmonious interaction between CdS and ZIF-8. The photocatalysts used for formic acid decomposition included pristine CdS nanoparticles, MCS, SCS-20, and SCS-40. The photocatalytic kinetic profiles were obtained. In comparison with pure CdS NPs, the MCSs demonstrate greater photocatalytic performance for $H_2$ production throughout the entire photocatalytic process. However, SCS-20 exhibits enhanced photocatalytic efficiency for $H_2$ production only during the initial 3.5 hours, and SCS-40 displays improved efficiency only during the first 2.5 hours.[136]

ZnS, a traditional metal sulfide, is widely recognized as a photocatalyst because of its high electron–hole pair generation rate and non-toxic nature. Song *et al.* aimed to develop bimetallic sulfides that integrate ZIF-derived sulfide structures with the capability for visible light absorption and effectively create bimetallic sulfides that integrate the structural benefits of ZIF-derived sulfides. In this study, a series of ZnS/$ZnIn_2S_4$ hybrid materials derived from ZIF-8 were successfully prepared by changing the amount of ZIF-8 to optimize the ratios of ZnS and $ZnIn_2S_4$. The hydrogen evolution performance of these materials was tested using TEOA as a hole scavenger. As shown in Fig. 4e, pure ZnS, owing to its wide band gap of 3.55 eV, showed no hydrogen production. Pure $ZnIn_2S_4$ achieved a $H_2$ generation rate of 118.4 $\mu$mol $L^{-1}$ $g^{-1}$ $h^{-1}$, which is significantly lower than the composites, indicating reduced charge transfer efficiency and faster electron–hole recombination. The ZnS/ZIS-$x$ composite exhibited improved hydrogen generation rates of 332 $\mu$mol $L^{-1}$ $g^{-1}$ $h^{-1}$, 453.4 $\mu$mol $L^{-1}$ $g^{-1}$ $h^{-1}$, and 286.3 $\mu$mol $L^{-1}$ $g^{-1}$ $h^{-1}$ as $x$ varied from 10 to 30, with ZnS/ZIS-20 delivering the

maximum output, demonstrating an optimal ratio maximizing HER performance. The hydrogen generation rates achieved by the ZnS/ZIS composites in this study were considerably greater than those of $ZnIn_2S_4$-based photocatalysts, highlighting a promising method for developing efficient HER catalysts.[86]

Transition metal phosphides (TMPs) are promising HER catalysts due to their excellent catalytic and electronic properties. Due to phosphorus sharing similar chemical properties with nitrogen, TMPs retain significant characteristics from multi-electron orbitals.[137,138] For instance, Jin and colleagues formulated a ternary novel photocatalyst comprising $WO_3$/$NiP_2$/ZIF-8, utilizing eosin-Y (EY) as a sensitizer, and 30% TEOA was used as a sacrificial agent. XRD, SEM, and TEM characterization revealed that $WO_3$ forms nanowires and ZIF-8 exhibits a well-defined dodecahedron morphology with good crystallinity. XPS confirmed the valence states of the elements, and UV–Vis DRS data indicated that the modified catalyst has a broader visible light absorption range than pure $WO_3$. The hybrid catalysts showed improved electron transfer, better charge separation, and longer lifetimes than the individual catalysts, enhancing $H_2$ production. The photocatalytic HER achieved an emission rate of 341.2 $\mu$mol $L^{-1}$ $g^{-1}$ $h^{-1}$ over 5 hours, which was 11.3 times higher than the pure $WO_3$. This improvement was attributed to the increased active sites and surface area presented by the $NiP_2$ co-catalyst in conjunction with ZIF-8. Additionally, $NiP_2$ aided in capturing photogenerated electrons, which then reacted with protons in the solution to produce hydrogen.[139]

ZIF-8-based nanomaterials have demonstrated significant potential in enhancing $H_2$ generation when integrated with materials like g-$C_3N_4$, carbon nanostructures, and other semiconductors. These hybrid systems improve charge separation, light absorption, and stability, leading to higher hydrogen evolution rates compared with pristine materials. By optimizing band gaps and enhancing interfacial interactions, these composites achieve impressive photocatalytic efficiency under light irradiation, highlighting their potential for sustainable hydrogen production. Table 2 summarizes the photocatalytic activity of ZIF-8 MOF-based nanocomposites in $H_2$ and $H_2O_2$ evolution.

### 4.2 $H_2O_2$ generation

Hydrogen peroxide ($H_2O_2$) is a clean oxidant and reductant commonly used in industrial chemistry and is also a promising high-energy fuel for fuel cells.[146] $H_2O_2$ can be produced through either a two-step single-electron reduction or a one-step two-electron reduction. In photocatalytic systems, holes in the VB oxidize $H_2O$ to $O_2$ and $H^+$, while $e^-$ in the CB reduce adsorbed $O_2$ to $H_2O_2$. The one-step, two-electron reduction is considered more efficient for producing $H_2O_2$ from a photoelectrochemical standpoint.[147–149]
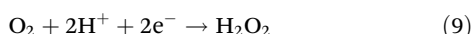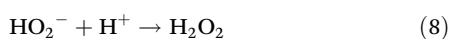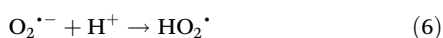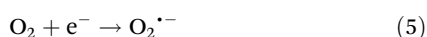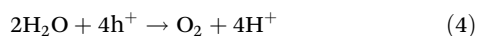
The two-step single-electron pathway mechanism involves the reactions discussed in eqn (4)–(8). Alternatively, the one-step, two-electron pathway mechanism involves the direct reaction of $O_2$ with two $H^+$ to produce $H_2O_2$ (eqn (9)). The overall

**Table 2** Summary of various ZIF-8 MOF-based nanocomposites and their performance in photocatalytic $H_2$ and $H_2O_2$ evolution

| Sl. no. | Photocatalytic application | Composite | Sacrificial agent | Light source | Activity | Quantum yield (%) | Ref. |
|---|---|---|---|---|---|---|---|
| 1 | $H_2$ evolution | $TiO_2$ @ZIF-8 | Methanol | 300 W Xe lamp | 254.2 μmol $g^{-1}$ $h^{-1}$ | 50.89 | 130 |
| 2 | | CdS/ZIF-8 | $Na_2S$ and $Na_2SO_3$ | 300 W Xe lamp | 2.10 mmol $g^{-1}$ $h^{-1}$ | — | 136 |
| 3 | | $MoS_2$@ZIF-8 | Methanol | — | 29.9 μmol $h^{-1}$ $g^{-1}$ | — | 135 |
| 4 | | ZIF-8 derived ZnCdS | $Na_2S$ and $Na_2SO_3$ | 300 W Xe lamp | 5680 μmol $g^{-1}$ $h^{-1}$ | — | 140 |
| 5 | | ZIF-8 derived ZnS | TEOA | 300 W Xe lamp | 3709.23 μmol $g^{-1}$ $h^{-1}$ | 0.014 | 141 |
| 6 | | CdS–ZnNi–ZIF-8 | $Na_2S$ and $Na_2SO_3$ | 300 W Xe lamp | 45.6 mmol $g^{-1}$ $h^{-1}$ | — | 142 |
| 7 | | Ag–AgBr/g-$C_3N_4$/ZIF-8 | TEOA | 300 W Xe lamp | 2058 μmol $g^{-1}$ $h^{-1}$ | 7.91 | 133 |
| 8 | | ZIF-8 derived $Co_3O_4$/ZnO | Glycerol | 500 W Xe lamp | 2241 μmol $g^{-1}$ $h^{-1}$ | — | 143 |
| 9 | | ZIF-8 derived ZnS/$ZnIn_2S_4$ | TEOA | 300 W Xe lamp | 453.4 μmol $g^{-1}$ $h^{-1}$ | — | 86 |
| 10 | | Co@ZIF-8/$TiO_2$ | Methanol | — | 13 mmol $g^{-1}$ $h^{-1}$ | — | 144 |
| 11 | | C-ZIF@g-$C_3N_4$ | TEOA | 300 W Xe lamp | 1238 μmol $g^{-1}$ $h^{-1}$ | — | 129 |
| 12 | | $WO_3$/$NiP_2$@ZIF-8 | TEOA | 300 W Xe lamp | 295.7 μmol $g^{-1}$ $h^{-1}$ | 50.8 | 139 |
| 13 | | ZIF-8/modified g-$C_3N_4$ | TEOA | 300 W Xe-lamp | 309.5 μmol $L^{-1}$ $g^{-1}$ $h^{-1}$ | — | 82 |
| 14 | $H_2O_2$ evolution | BiOBr/ZIF-8/ZnO | — | LED light | 116 mmol $L^{-1}$ $g^{-1}$ | — | 145 |
| 15 | | ZIF-8/$C_3N_4$ | — | Visible light ($\lambda \geq 420$ nm) | 2641 μmol $h^{-1}$ $g^{-1}$ | 19.54 | 131 |

photocatalytic reaction can be summarized as follows (eqn (10)):

$$2H_2O + 4h^+ \rightarrow O_2 + 4H^+ \tag{4}$$

$$O_2 + e^- \rightarrow O_2^{\cdot -} \tag{5}$$

$$O_2^{\cdot -} + H^+ \rightarrow HO_2^{\cdot} \tag{6}$$

$$HO_2^{\cdot} + e^- \rightarrow HO_2^- \tag{7}$$

$$HO_2^- + H^+ \rightarrow H_2O_2 \tag{8}$$

$$O_2 + 2H^+ + 2e^- \rightarrow H_2O_2 \tag{9}$$

$$2H_2O + O_2 \xrightarrow{h\vartheta} 2H_2O_2 \quad \Delta G_0 = 117\,\text{kJ}\,\text{mol}^{-1} \tag{10}$$

The photocatalytic production of $H_2O_2$ from $H_2O$ and $O_2$ is an uphill reaction with a standard Gibbs free energy change ($\Delta G_0$) of 117 kJ $mol^{-1}$.

Zhao *et al.* showed that ZIF-8/$C_3N_4$ composite is a highly effective photocatalyst for producing $H_2O_2$ by a two-channel pathway, *i.e.*, both oxygen reduction and water oxidation reaction. The SEM image of $C_3N_4$ displays a sheet-like structure, while the ZIF-8 (Fig. 4f) display a rhombic dodecahedral shape with an approximate size of 100 nm. ZIF-8 exhibits significant nitrogen adsorption at minimal relative pressures, suggesting the existence of numerous micropores, which is further supported by the pore size distribution analysis. Transient photovoltage (TPV) measurements provide insight into the photocatalytic water-splitting mechanism for $H_2O_2$ production using the ZIF-8/$C_3N_4$ composite. Fig. 4g illustrates that the ZCN sample (black line) exhibits a notably higher photocurrent response, signifying an increased accumulation of photoinduced charges on the surface. This implies improved electron–hole separation efficiency in ZCN. Under an $O_2$ atmosphere, ZCN's photocurrent decreases more than under $H_2$, indicating rapid oxygen reduction and water oxidation as the rate-determining step. The composite facilitates $H_2O_2$ production through simultaneous $O_2$ reduction and $H_2O$ oxi-dation. The proposed reaction mechanism suggests that in the ZCN composite, visible light excites $C_3N_4$ to separate electron–hole pairs, where ZIF-8 enhances visible light absorption, and facilitates $O_2$ adsorption for efficient $H_2O_2$ production, and its porous structure aids in mass transfer and prevents catalyst poisoning (Fig. 4h). Unlike ZIF-8 alone, which shows no activity, and $C_3N_4$, which produces only 67.50 μmol $h^{-1}$ $g^{-1}$, the composite significantly enhances efficiency by achieving 2461 μmol $h^{-1}$ $g^{-1}$. It demonstrates excellent stability, with re-usability for at least five cycles under visible light, with only a slight performance decline due to catalyst loss, and the composite maintains good morphological stability throughout the cycles.[131]

Bismuth-based materials are commonly employed in photocatalytic studies due to their open structural framework and favorable band gap. Among them, BiOBr is considered an excellent catalyst support because of its strong stability, affordability, responsiveness to visible light, and diverse microstructural properties. To address issues like the agglomeration of ZIF-8, Yang *et al.*[150] employed ZnO/ZIF-8 hybrid photocatalyst under UV light irradiation, which can decompose 98.17% RhB in 12 min. Building on this approach, Han *et al.* synthesized BiOBr/ZIF-8/ZnO ternary composite and demonstrated effective $H_2O_2$ generation under LED lamp irradiation, reducing ZIF-8 aggregation and enhancing charge carrier separation. The DRS spectra reveal the UV light responsiveness of BiOBr, ZIF-8, ZZ-110, and BZ-9, with the latter showing a redshift in absorption edges. BZ-9's edge extended to ~500 nm, indicating a broader light response and visible light interaction. Tauc plot analysis calculated the band gaps as 2.70 eV for BiOBr and 2.91 eV for ZZ-110. Electrochemical tests (Fig. 5a) showed that BZ-9 produced an enhanced photocurrent compared with the other catalysts, suggesting better optical absorption and enhanced electron–hole separation efficiency. The LSV curve demonstrated that BZ-9 had the lowest potential, implying a reduced electron–hole recombination rate (Fig. 5b). Mott–Schottky analysis showed flat band potentials of −0.117 for BiOBr and −1.007 for ZZ-110. BiOBr
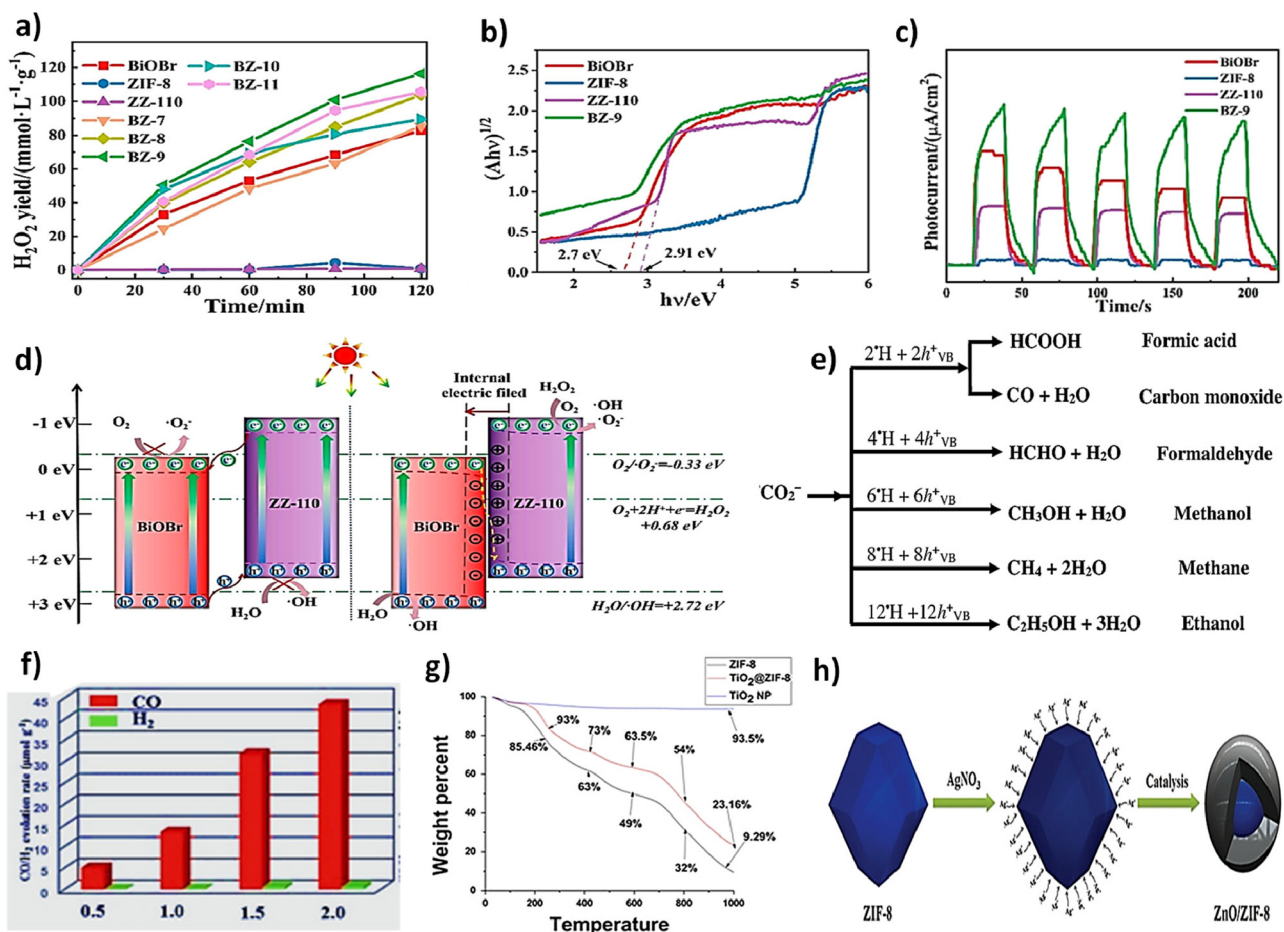
**Fig. 5** (a) $H_2O_2$ production capacity, (b) the band gaps and (c) Nyquist plots of BiOBr, ZIF-8, ZZ-110, and BZ-9. (d) The photocatalytic mechanisms of BiOBr and ZZ-110 involve two distinct heterojunction types: type II heterojunction and an S-scheme heterojunction [reproduced from ref. 145 with the permission from MDPI, copyright 2023]. (e) The total pathways for production of the main products of photocatalysis of $CO_2$ [reproduced from ref. 151 with the permission from Elsevier, copyright 2016]. (f) Time–yield plots of CO and $H_2$ over $TiO_2$/ZIF-8-G2 composites [reproduced from ref. 152 with the permission from The Royal Society of Chemistry, copyright 2021]. (g) TGA of ZIF-8, $TiO_2$@ZIF-8 and $TiO_2$ NPs in air [reproduced from ref. 153 with the permission from Elsevier, copyright 2015]. (h) The synthetic procedure of ZnO/ZIF-8 hybrid photocatalysts [reproduced from ref. 154 with the permission from Elsevier, copyright 2016].

and the composites generated significant amounts of $H_2O_2$, with BZ-9 exhibiting the greatest production of 116 mmol $L^{-1}$ $g^{-1}$ within two hours, 1.4 times greater than pristine BiOBr (Fig. 5c). The photocatalytic mechanism proposed that BiOBr and ZZ-110 establish a conventional type II heterojunction, as illustrated in Fig. 5d. After four cycles, the $H_2O_2$ evolution of BZ-9 decreased to 109 mmol $L^{-1}$ $g^{-1}$, representing good stability. HCOOH influenced $H_2O_2$ generation by capturing holes, oxidizing to $HCOO^•$, which further reacted to form $^•OH$ and $H_2O_2$, with CB electrons at ZZ-110 to reduce $O_2$ to $H_2O_2$.[145]

By integrating ZIF-8 with materials like $C_3N_4$, BiOBr, and ZnO, the overall photocatalytic performance is greatly enhanced compared with the individual components, showcasing excellent stability, reusability, and scalability for practical applications. These findings underscore the importance of material design in optimizing photocatalytic processes for energy and environmental applications.

### 4.3 $CO_2$ reduction

$CO_2$ is a highly stable molecule ($\Delta G^{\circ} = -400$ kJ $mol^{-1}$) with a linear structure comprising two double bonds between oxygen and carbon atoms. This stability and its large LUMO–HOMO energy gap of 13.7 eV and high electron affinity of $-0.6 \pm 0.2$ eV make it difficult to convert $CO_2$ into valuable chemicals without catalysts and energy input. The conversion process is hindered by thermodynamic and kinetic limitations.[155,156] However, when $CO_2$ adsorbs onto a photocatalyst surface, its linear structure bends, lowering the energy barrier and increasing reactivity by reducing the LUMO level. This adsorption initiates sequential reactions through one-electron transfers involving electron or proton transfers that break C–O bonds and form new C–H bonds. A reducing agent, such as $H_2O$, $H_2$, $CH_4$, or $CH_3OH$, is needed to supply hydrogen for producing hydrocarbons through photocatalysis. The pathways for photo-

catalytic $CO_2$ reduction depend on the reductant used. Carbon-free reductants like $H_2O$ and $H_2$ typically yield C1 products, whereas carbon-containing reductants like $CH_4$ and $CH_3OH$ can produce C2 and C3 products. Common products from $CO_2$ photoreduction include CO, HCOOH, HCHO, $CH_3OH$, $CH_4$, and $C_2H_5OH$.[157–159] Fig. 5e illustrates the electrons, oxidizing holes, and protons ($H^+$) required for forming these main products.[151]
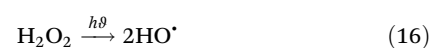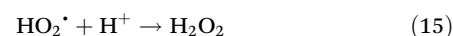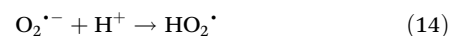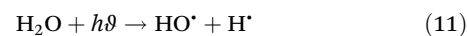
As $TiO_2$ has strong oxidative power, high chemical stability, and non-toxicity, Yan *et al.* synthesized a composite using ZIF-8 and $TiO_2$ through grinding and solid-synthesis methods. These composites were employed for the photocatalytic reduction of $CO_2$. XPS confirmed the appearance of Zn 2p, N 1s, C 1s, Ti 2p, and O 1s in $TiO_2$/ZIF-8-G2. Peaks at 458.6 eV and 464.3 eV correspond to $Ti^{4+}$ (Ti $2p_{3/2}$ and Ti $2p_{1/2}$), while peaks at 1022.1 eV and 1045.1 eV are allotted to Zn $2p_{3/2}$ and Zn $2p_{1/2}$. The $CO_2$ photoreduction efficiency is attributed to $TiO_2$/ZIF-8-G2, with its photocatalytic efficiency at specific time intervals reaching 5.04, 13.38, 31.85, and 43.49 mmol $g^{-1}$, as depicted in Fig. 5f. The UV-DRS spectra indicate that $TiO_2$/ZIF-8-G2 exhibits a broader absorption band and an extended absorption edge near 400 nm, suggesting enhanced light absorption. The EIS results reveal that $TiO_2$/ZIF-8-G2 has the shortest radius within the $TiO_2$/ZIF-8-G$X$ photocatalysts, indicating superior conductivity and more efficient photogenerated electron transfer. This aligns with the photocurrent and $CO_2$ photoreduction performance. Consequently, a CO production rate of 21.74 mmol $g^{-1}$ $h^{-1}$ with a remarkable 99% selectivity was attained in the solid-gas system without the use of sacrificial agents or photosensitizers. The group's previous highest CO generation rate was 10.67 mmol $g^{-1}$ $h^{-1}$, achieving 90% selectivity.[152]

$SnO_2$, known for its high oxidation potential and electron–hole capture, has been widely used in various fields. Wang *et al.* synthesized T-ZIF-8/$SnO_2$ spherical photocatalysts *via* the sol–gel method for $CO_2$ reduction, forming type-II heterojunctions. HRTEM showed that T-ZIF-8 retained its framework with spherical deformation, while $SnO_2$ appeared as ~9 μm particles, covered by T-ZIF-8. The materials exhibited type-IV isotherms with H3 hysteresis loops, indicating slit pores from nanoparticle aggregation. A reduced PL intensity in T-ZIF-8/$SnO_2$ compared with T-ZIF-8 indicated slower electron–hole recombination, attributed to the heterojunction's multiple charge transfer pathways. This enhanced charge separation, reduced recombination, and improved charge carrier transport, increasing active sites and reducing the bandgap. Under simulated sunlight, T-ZIF-8/$SnO_2$ demonstrates exceptional photocatalytic performance, achieving a $CO_2$ generation rate of 16.6 μmol $g^{-1}$ $h^{-1}$, which is 1.4 and 4.9 times greater than the pristine $SnO_2$ and T-ZIF-8, respectively. Furthermore, it attains a $CH_4$ generation rate of 14.7 μmol $g^{-1}$ $h^{-1}$, which is 1.9 and 6.1 times higher than that of pure $SnO_2$ and T-ZIF-8. These findings verify that the heterojunction significantly enhances both photocatalytic $CO_2$ reduction efficiency and $CH_4$ selectivity.[160]

$CO_2$ reduction using ZIF-8-based photocatalysts highlights significant advancements in overcoming the inherent stability of $CO_2$ and promoting its conversion into valuable chemicals. The formation of heterojunctions in these composites plays a major role in increasing photocatalytic activity by facilitating charge transfer and enhancing the overall conversion of $CO_2$ into useful products such as CO and $CH_4$ without the need for sacrificial agents. The photocatalytic performance of ZIF-8 MOF-based nanocomposites in $CO_2$ reduction and dye and drug degradation has been summarized in Table 3.

## 4.4 Dye degradation

The elimination of dyes from industrial wastewater is essential due to their harmful effects on aquatic life and their potential carcinogenic risks to humans. Traditional dye removal methods often fail to achieve complete degradation and produce significant amounts of suspended solids. Therefore, an efficient process that can fully degrade dyes with minimal waste is critically needed. Photocatalysis is a promising approach for degrading various toxic and organic pollutants in wastewater. The detailed mechanism of photocatalysis is explained in the following reactions.[184–186]

$$H_2O + h\vartheta \rightarrow HO^\bullet + H^\bullet \quad (11)$$

$$HO^\bullet + O_2 \rightarrow HO_2^\bullet \quad (12)$$

$$O_2 + e^- \rightarrow O_2^{\bullet-} \quad (13)$$

$$O_2^{\bullet-} + H^+ \rightarrow HO_2^\bullet \quad (14)$$

$$HO_2^\bullet + H^+ \rightarrow H_2O_2 \quad (15)$$

$$H_2O_2 \xrightarrow{h\vartheta} 2HO^\bullet \quad (16)$$

Finally, the dye reacts with an $HO^\bullet$ radical to form intermediate products and end products:

$$HO^\bullet + dye \rightarrow Intermediates \rightarrow CO_2 + H_2O$$
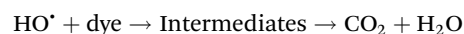
$TiO_2$ is commonly implemented as a photocatalyst because of its excellent activity and robust chemical and photochemical stability.[150] Chandra *et al.* embedded $TiO_2$ nanotubes within ZIF-8 to fabricate a $TiO_2$@ZIF-8 for the degradation of RhB and MB dyes. FESEM and HRTEM images show that the composite retains the hexagonal morphology of ZIF-8, where $TiO_2$ nanoparticles appear as dark spots within the ZIF-8 cages. According to the UV-DRS spectral analysis, the composite exhibited a flat band structure, identical to what is seen with $TiO_2$ nanoparticles, with a slight reduction in the band gap from about 3.35 eV to 3.25 eV, due to changes in the microenvironment within the ZIF-8 framework, and amplified the photocatalytic performance of the $TiO_2$ NPs encapsulated within the ZIF-8 framework. Surface analysis using BET adsorption measurement revealed a decrease in surface area ranges from 1432.91 $m^2$ $g^{-1}$ to 253.882 $m^2$ $g^{-1}$ when comparing the isotherms of the

**Table 3**  Summary of various ZIF-8 MOF-based nanocomposites and their performance on photocatalytic $CO_2$ reduction, dye, and drug degradation

| | Photocatalytic application | Composite | Band gap (eV) | Light source | Activity | Ref. |
|---|---|---|---|---|---|---|
| 1 | CO$_2$ reduction | TiO$_2$/ZIF-8 | 1.97 | LED lamp, 40 W | CO = 21.74 μmol g$^{-1}$ h$^{-1}$ | 161 |
| 2 | | ZnO/ZIF-8 | 3.23 | Hg lamp, 125 W | CH$_3$OH = 6843.12 μmol g$^{-1}$ | 162 |
| 3 | | Pt/ZIF-8 | 4.21 | Hg lamp, 125 W | CH$_3$OH = 5365.01 μmol g$^{-1}$ | 162 |
| 4 | | Cu/ZIF-8 | 2.09 | Hg lamp, 125 W | CH$_3$OH = 426.02 μmol g$^{-1}$ | 162 |
| 5 | | Au/ZIF-8 | 1.69 | Hg lamp, 125 W | CH$_3$OH = 232.20 μmol g$^{-1}$ | 162 |
| 6 | | Cu–TiO$_2$/ZIF-8 | — | UV lamp, 320–480 nm | CH$_3$OH = 4.88 μmol g$^{-1}$ | 163 |
| 7 | | TiO$_2$/ZIF-8 | — | UV lamp, 8 W | CO = 0.53 mmol g$^{-1}$ h$^{-1}$, CH$_4$ = 0.18 mmol g$^{-1}$ h$^{-1}$ | 164 |
| 8 | | CdS/ZIF-8 | 2.41 | Xe lamp, 300 W | CO = 32.13 μmol h$^{-1}$ | 161 |
| 9 | | CdSe QD@ZIF-8 | — | Xe lamp, 300 W | CO = 3.526 μmol g$^{-1}$ h$^{-1}$, CH$_4$ = 0.102 μmol g$^{-1}$ h$^{-1}$ | 165 |
| 10 | Drug degradation | ZIF-8/TiO$_2$ | 2.98 | 300 W Xe lamp | TC = 90% in 40 min | 93 |
| 11 | | ZIF-8/Cu$_2$O | 4.31 | Solar light | TC = 84.1% in 120 min | 166 |
| 12 | | ZIF-8 derived CuO/ZnO | — | 300 W Xe lamp | TC = 87% in 60 min | 167 |
| 13 | | ZIF-8/MoS$_2$ | 1.05 | 300 W Xe lamp | Ciprofloxacin = 93.2% in 180 min | 168 |
| 14 | | ZIF-8/g-C$_3$N$_4$ | 2.73 | — | TC = 87.6% in 40 min | 143 |
| 15 | | Ag/AgCl@ZIF-8/g-C$_3$N$_4$ | — | Visible light | Levofloxacin = 94.5% in 60 min | 169 |
| 16 | Dye degradation | CuONPs/ZIF-8 | 4.93 | Sunlight | Rh6G = 96.5% in 105 min | 57 |
| 17 | | MnO$_2$@ZIF-8 | 5.46 | 300 W xenon lamp | RhB > 96.0% | 170 |
| 18 | | ZIF-8/NiFe$_2$O$_4$ | — | 500 W halogen lamp | MB = 94% in 120 min | 92 |
| 19 | | ZIF-8/Fe$_2$O$_3$ | — | 500 W Xe lamp | Reactive red = 94% | 171 |
| 20 | | ZnO@ZIF8 | 3.31 | Metal halide lamp/575 W | MB = 97.65% in 45 min | 154 |
| 21 | | ZIF-8 derived ZnO | — | UV lamp/18 W | MB = 76% in 60 min | 172 |
| 22 | | RGO/black TiO$_2$/2D-ZIF-8 | — | Visible light | MB = 0.0232 min, DH = 0.0118 min | 173 |
| 23 | | MoO$_3$@ZIF-8 | — | PL-XQ 350 W xenon | MB = 95% in 300 min | 174 |
| 24 | | CuO–ZnO/ZiF-8 | 1.96 | Solar light | AO7 = 98.1% in 100 min | 175 |
| 25 | | ZIF-8/g-C$_3$N$_4$ | 2.80 | Xe lamp/300 W | RhB = 99.8% in 60 min | 58 |
| 26 | | Ag-doped ZIF-8 | 3.2 | Visible LED light | MO = 100%, RhB = 93% in 30 min | 176 |
| 27 | | ZIF-8@AgNPS | 5.13 | UV–vis light | CR = 100% | 177 |
| 28 | | Ag/AgCl@ZIF-8 | 3.3 | Hg lamp/175 W | MB = 100% in 90 min | 178 |
| 29 | | AgCl/Ag@ZIF-8 | — | Xe lamp/210 W | RhB = 86% in 60 min | 179 |
| 30 | | ZIF-8/Ag$_2$S | 3.24 | 100 W Xe and 100 W LED | RhB = 100% in 75 min | 180 |
| 31 | | CdSNPs@ZIF-8 | 2.95 | UV–visible | MB = 83.2% in 120 min | 181 |
| 32 | | ZIF-8/Zn-Al LDH | — | UV light/70 W | MB = 58% in 180 min | 182 |
| 33 | | ZIF-8@CQD | 4.95 | 300 W Xe lamp | MB = 91% | 183 |
| 34 | | TiO$_2$@ZIF-8 | 3.25 | Solar light | MB = 87.5%, RhB = 64.85%. 120 min | 153 |

ZIF-8 framework and the composite. This observation confirmed the coating of TiO$_2$ NPs within the framework pores, resulting in reduced void space accessible to N$_2$ gas molecules. Thermal gravimetric analysis indicated high stability of both ZIF-8 and TiO$_2$@ZIF-8 up to 236 °C and 254 °C, respectively, in atmospheric air and up to 240 °C and 270 °C under an inert N$_2$ atmosphere. Beyond these temperatures, the frameworks gradually decomposed, with a gradual decline observed until approximately 670 °C (Fig. 5g). After 2 hours of catalysis, complete elimination of dye color was achieved, and the removal rate of RhB and MB by TiO$_2$@ZIF-8 was 64.85% and 87.5%, respectively. In comparison, TiO$_2$ and ZIF-8 alone exhibited lower degradation rates, with methylene blue degradation at 29% and 86.25% and rhodamine-B degradation at 53.6% and 50%, respectively. Notably, TiO$_2$@ZIF-8 maintained a high recycling rate, demonstrating almost the same efficiency even in the fifth catalytic cycle. In contrast, TiO$_2$ nanotubes exhibited significantly reduced catalytic efficiency after just the second degradation cycle.[153]

TiO$_2$ thin films doped with Fe, Cu, Ce, or Zn were designed to enhance the photocatalytic efficiency of the nanocomposite.[187] Considering this, Yurtsever et al. examined the effects of crystallization time and the amount of ZIF-8 on the photocatalytic performance of Cu–TiO$_2$/ZIF-8. These films exhibited superior light absorption compared with other ZIF-8-coated TiO$_2$ films and bare ZIF-8. This enhanced light absorption likely boosts photocatalytic activity, suggesting that using undoped or doped TiO$_2$ thin films as supports can enhance the photocatalytic efficiency of ZIF-8. They observed that decreasing the ZIF-8 loading and shortening the development time led to enhanced photocatalytic performance. Specifically, nanocomposites with 5% ZIF-8 loading and a growth time of 15 minutes exhibited the greatest photocatalytic efficiency, with a first-order rate constant 4 times and 1.4 times greater than that of pristine ZIF-8 and Cu–TiO$_2$, respectively. However, increasing the ZIF-8 content to 46% led to aggregate clumping, which decreased the photocatalytic efficiency. The ZIF-8/TiO$_2$ nanocomposite thin films, which were synthesized using 1% copper or 1% cerium-doped TiO$_2$ as substrates, displayed the highest activity for MB degradation. Both films removed 19% of the dye under 254 nm LED light in 1 hour and achieved 36% and 29% dye removal, respectively, under 365 nm LED light in the same time frame.[188]

He *et al.* developed a ternary system comprising RGO/black $TiO_2$/2D-ZIF-8 for the degradation of MB. The integration of 2D-ZIF-8 into the system enhanced the capacity of dye adsorption and facilitated *in situ* accumulation. The three-component composite exhibited dual diverse interfaces, which were crucial for the movement and segregation of charge carriers. The rate constant for MB photocatalytic decomposition was found to be 0.0232 $min^{-1}$, which is 3.3 times higher than black $TiO_2$ alone. The ternary GO/B-$TiO_2$/2D-ZIF-8 composites showed the smallest semicircle diameter, indicating that RGO/ B-$TiO_2$/2D-ZIF-8 has the maximum charge carrier mobility. The photocatalytic degradation mechanism explains that photogenerated electrons on black $TiO_2$ surfaces struggle to react with $O_2$ to form $O_2^{\cdot-}$, as the redox potential of the $O_2/O_2^{\cdot-}$ couple (−0.33 eV) is lower than the CB energy of black $TiO_2$ (−0.27 eV). Furthermore, the redox potential of the $H_2O/OH^-$ couple (2.53 eV) exceeds the VB energy of ZIF-8 (0.34 eV), making it inefficient for photogenerated holes to convert $H_2O$ into $OH^{\cdot}$. Consequently, the holes directly interact with MB during the photodegradation process. The excellent electrical conductivity of RGO also contributes to the efficient separation of electron–hole pairs and lowers the recombination rate, which in turn improves the photodegradation of MB.[173]

Recently, ZnO photocatalysts have attracted significant attention owing to their non-toxicity, stability, cost-effectiveness, and efficient photocatalytic activity. Yang *et al.* introduced an innovative method for producing ZIF-8/ZnO composite photocatalysts *via* a micro-catalysis approach, utilizing ZIF-8 as the reactant and $AgNO_3$ as the catalyst, varying the concentration of $AgNO_3$ (Fig. 5h). The treatment with a 25 mM $AgNO_3$ solution resulted in the edges of the ZIF-8 surface becoming spherical, leading to a reduction in particle size. Increasing the $AgNO_3$ concentration to 50 mM further decreased the particle size to approximately 200 nm, with a more pronounced spherical morphology. The composite synthesized with a 50 mM $AgNO_3$ solution (designated as ZIF-8/ ZnO (50)) achieved supreme decomposition performance at approximately 98.17% compared with its counterparts synthesized with 100 mM and 25 mM of $AgNO_3$. Additionally, the composite demonstrated robust photostability, retaining a photocatalytic activity of 95.54% after reuse for four cycles as ZnO/ZIF-8(50) showcased high photocatalytic stability, with only a 2.63% reduction in activity after four cycles, attributed primarily to inevitable catalyst loss. Consequently, ZnO/ZIF-8 (50) demonstrates commendable preparation and reusability properties.[154]

ZnO, an n-type semiconductor possessing conductivity between $10^{-7}$ and $10^{-3}$ S $cm^{-1}$ and a binding energy of 60 meV, pairs effectively with CuO, a p-type semiconductor possessing a narrow band gap and conductivity around $10^{-4}$ S $cm^{-1}$. Saravanan *et al.* synthesized CuO/ZnO nanocomposites, followed by Abdollahi and collaborators, used a precipitation method to create a CuO–ZnO/ZIF-8 photocatalyst, which was tested for the photocatalytic decomposition of methylene blue, malachite green and Acid Orange 7. The sample with 20 wt% ZIF-8 was found to have a reduced band gap energy of 1.96 eV,

compared with the band gap energies of ZIF-8 and CuO–ZnO, as determined by DRS analysis. Additionally, incorporating ZIF-8 into the CuO–ZnO heterojunction increased the specific surface area from 12.3 $m^2$ $g^{-1}$ to 22.2 $m^2$ $g^{-1}$. This increase allowed the photocatalyst to adsorb a larger amount of dye, which was then decomposed under visible light, and the study found that increasing photocatalyst loading from 0.5 to 1 g $L^{-1}$ improved the photodecomposition rate, attributed to the increased number of active sites. The CuO–ZnO/ZIF-8-20 photocatalyst demonstrated a photocatalytic activity of 51%, 98.1%, and 59% for removing malachite green, Acid Orange 7, and Methylene blue at pH 7.[175]

Cao *et al.* effectively coated $MnO_2$ onto ZIF-8 through a reaction process. The incorporation of $MnO_2$ NPs onto ZIF-8 ensured their even dispersion, enhancing the active surface area (Fig. 6a). The $MnO_2$@ZIF-8 nanoparticles display a notable size enlargement as compared with the original ZIF-8. The sizes of the $MnO_2$@ZIF-8 NPs are 605 ± 60 nm, 410 ± 45 nm, and 205 ± 30 nm at $I_6R_4$ concentrations of 0.1 mM, 0.5 mM, and 1.0 mM, respectively (Fig. 6b). ZIF-8 and the composite analyzed *via* $N_2$ adsorption/desorption exhibited type I nitrogen isotherms, indicating micropores at low pressures and mesopores at relative pressures above 0.9. Consequently, the synthesis of the ZIF-8@$MnO_2$ heterojunction facilitated optimized charge carrier separation, leading to the generation of abundant free radicals like OH. Additionally, the $MnO_2$@ZIF-8 NPs have a zeta potential ($\zeta$) value of 15–23 mV, which is noticeably lower than that of the ZIF-8 crystals. In a Fenton-like process, the resulting ZIF-8@$MnO_2$ hybrid served as a photocatalyst for the decomposition of RhB and reached over 96.0% within 120 minutes, significantly outperforming the 63% degradation rate achieved with pristine ZIF-8. The recyclability of $MnO_2$@ZIF-8 nanoparticles in the photocatalytic degradation of RhB indicates that the ratio remained above 80% after five cycles, demonstrating excellent recycling stability and reusability. These promising outcomes stemmed from the porous structure of ZIF-8s, facilitating the adsorption of more RhB molecules.[170]

Faraji and associates harnessed the magnetic characteristics of $NiFe_2O_4$ to develop a ZIF-8/$NiFe_2O_4$ composite, which allows for convenient separation from the reaction mixture. This composite photocatalyst was scrutinized for its efficacy in decomposing MB under a 500 W halogen lamp, with visible light (≥400 nm) as the irradiation source. The magnetic performance of $NiFe_2O_4$ and the Z/NFO-30 composite was analyzed under an external magnetic field of ±1.5T at ambient temperature. Pure $NiFe_2O_4$ nanoparticles exhibited superparamagnetic behavior with a saturation magnetization (Ms) of approximately 38.54 emu $g^{-1}$. In contrast, the composite, which includes ZIF-8 integrated with $NiFe_2O_4$, showed a lower Ms of about 10 emu $g^{-1}$, as shown in Fig. 6c. This reduction in Ms is attributed to the integrating of ZIF-8 into the $NiFe_2O_4$ matrix, affecting the total mass and magnetic properties. Among the samples, Z/NFO-30 displayed the weakest emission peak intensity, indicating a reduced recombination rate of photoexcited charge carriers. Their research revealed that the
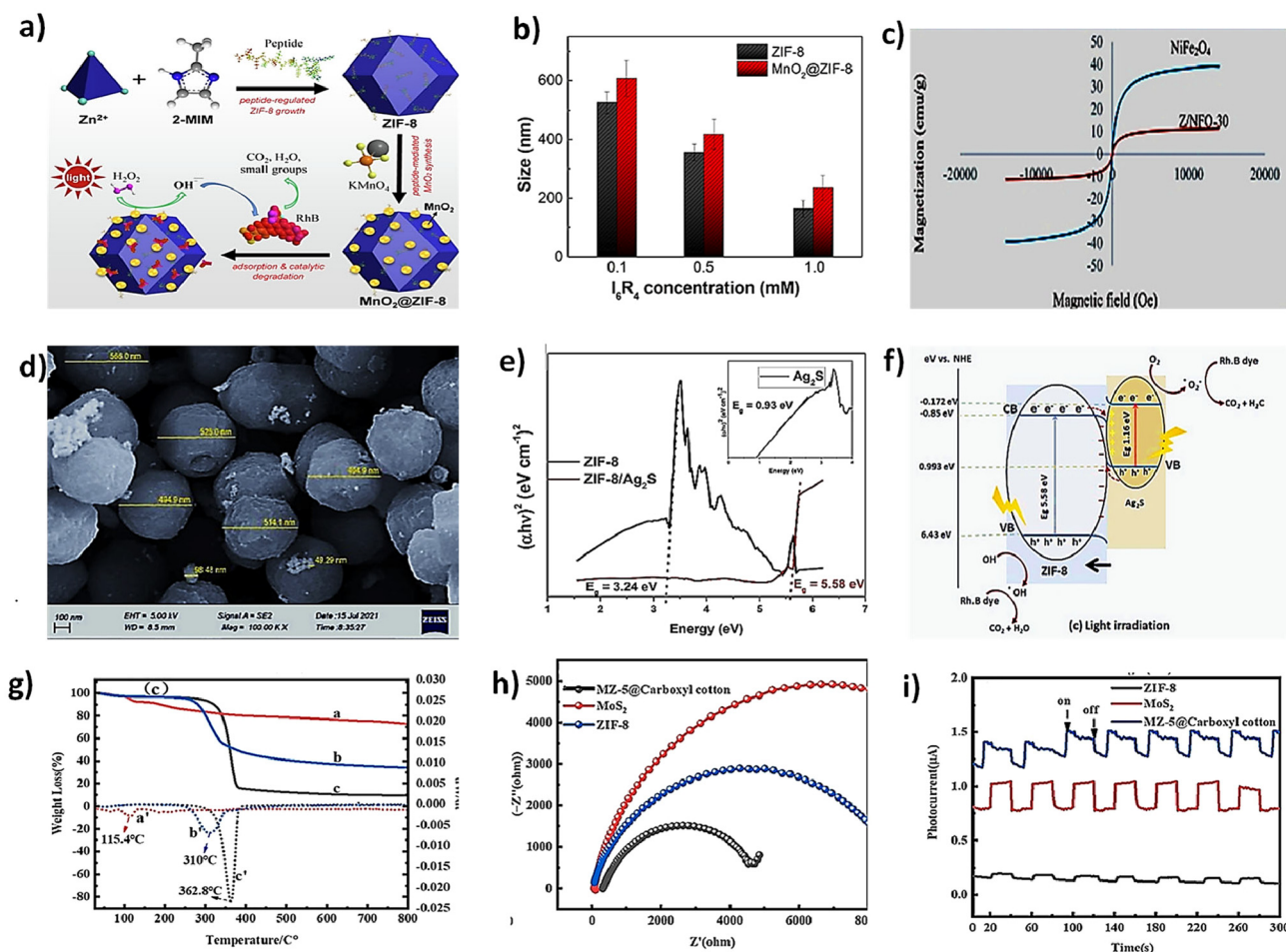
**Fig. 6** (a) Fabrication of $MnO_2$@ZIF-8 core–shell nanocomposites. (b) Size (hydrodiameter) distribution of the ZIF-8 crystals and the $MnO_2$@ZIF-8 nanocomposites prepared at varied peptide concentrations [reproduced from ref. 170 with the permission from Elsevier, copyright 2021]. (c) Magnetic hysteresis curve of $NiFe_2O_4$ nanoparticles and Z/NFO-30 composite [reproduced from ref. 92 with the permission from Elsevier, copyright 2020]. (d) FE-SEM of ZIF-8/$Ag_2S$. (e) Optical bandgap for ZIF-8, $Ag_2S$, and ZIF-8/$Ag_2S$ by using Tauc plots. (f) S-scheme mechanism of ZIF-8/$Ag_2S$ photocatalyst under vis-light irradiation [reproduced from ref. 180 with the permission from Elsevier, copyright 2016]. (g) TG and DTG curves of $MoS_2$/ZIF-8 composite (a and a'); MZ-5@Carboxyl cotton (b and b'); pristine cotton fabric (c and c'). (h) EIS plots of MZ-5@Carboxyl cotton, $MoS_2$ and ZIF-8 (i) transient photocurrent responses of $MoS_2$, ZIF-8 and MZ-5@Carboxyl cotton [reproduced from ref. 189 with the permission from Elsevier, copyright 2016].

photocatalyst, formulated with 30 wt% $NiFe_2O_4$, exhibited the most robust photocatalytic activity, achieving a degradation efficiency of 94% within 120 minutes. Additionally, its magnetic nature enabled the composite to be renewed and reutilized for four cycles while maintaining a degradation efficiency of 90%.[92]

Metal sulfides are highly effective photocatalysts because of their strong charge carrier migration capabilities, excellent light absorption properties, suitable band structure, and abundance of exposed active sites. Jabbar and co-authors examined the photocatalytic degradation of RhB using a ZIF-8/$Ag_2S$ nanocomposite photocatalyst, where $Ag_2S$ nanoparticles were effectively dispersed on the ZIF-8 surface, creating a high-efficiency heterogeneous catalyst through the co-precipitation method. The morphology of the composite, as shown in Fig. 6d, revealed semicubic particles with a slight shape change from pure ZIF-8, indicating successful $Ag_2S$ nano-

particle precipitation. UV–vis absorption spectra demonstrated improved visible light absorption in the ZIF-8/$Ag_2S$ composite due to its reduced band gap, as further confirmed by the band gap values of 5.58 eV for ZIF-8, 0.93 eV for $Ag_2S$, and 3.24 eV for the composite (Fig. 6e). This narrowed band gap is attributed to the effective dispersion of $Ag_2S$ within the ZIF-8 structure. In RhB degradation tests, the ZIF-8/$Ag_2S$ nanocomposite achieved complete photodegradation within 75 minutes in an airlift reactor, compared with 120 minutes in a batch reactor, with enhanced performance due to improved mixing and increased dissolved oxygen. The study also explored the impact of catalyst dosage, with the composite showing 100% degradation efficiency at optimal loading compared with 51.6% for ZIF-8 and 39.7% for $Ag_2S$ alone, and it follows an S-scheme heterojunction photocatalytic mechanism (Fig. 6f). Finally, the composite demonstrated excellent stability and reusability, maintaining high photodegradation efficiency over five cycles,

due to the dispersion of $Ag_2S$ aggregates on the ZIF-8 surface.[180]

$MoS_2$, with its low band gap and reactive edge, features a "sandwich" S–Mo–S structure that enhances the visible light response, making it effective for boosting the photocatalytic efficiency of ZIF-8.[190] Chen and his team effectively fabricated ZIF-8 on carboxylated cotton cloth and then grew $MoS_2$ on the ZIF-8 surface, creating an $MoS_2$/ZIF-8/carboxyl cotton composite. Fig. 6g shows TG and DTG curves, where $MoS_2$/ZIF-8 powder and MZ-5@Carboxyl cotton display distinct weight losses due to decomposition, leaving final residues of ∼76.5% and ∼34.1%, respectively. XPS analysis revealed that S, Mo, Zn, C, O, and N are the key elements in MZ-5@Carboxyl cotton, with strong peaks indicating the presence of S 2p, Mo 3d, and Zn 2p, confirming that $MoS_2$ is closely integrated with the ZIF-8 surface. The EIS spectra for the composite (Fig. 6h) dis-

played a smaller arc radius, indicating enhanced light-induced charge transfer due to $MoS_2$/ZIF-8 heterostructures. This was supported by the highest electron–hole separation efficiency observed in the photocurrent response (Fig. 6i) and confirmed by Mott–Schottky analysis (Fig. 7a), identifying MZ-5@Carboxyl cotton as an n-type semiconductor. This composite efficiently degraded methylene blue (MB), achieving approximately 99.8% degradation of the aqueous solution after 21 minutes of visible-light exposure. The fabric with five layers of ZIF-8 demonstrated the highest MB degradation efficiency and retained approximately 94.8% of its photocatalytic activity after six recycling cycles.[189]

Doping MOFs with active agents enhances photocatalytic efficiency. The challenge lies in developing cost-effective, stable doped nanomaterials with precisely-controlled properties for efficient visible light absorption. In light of this,
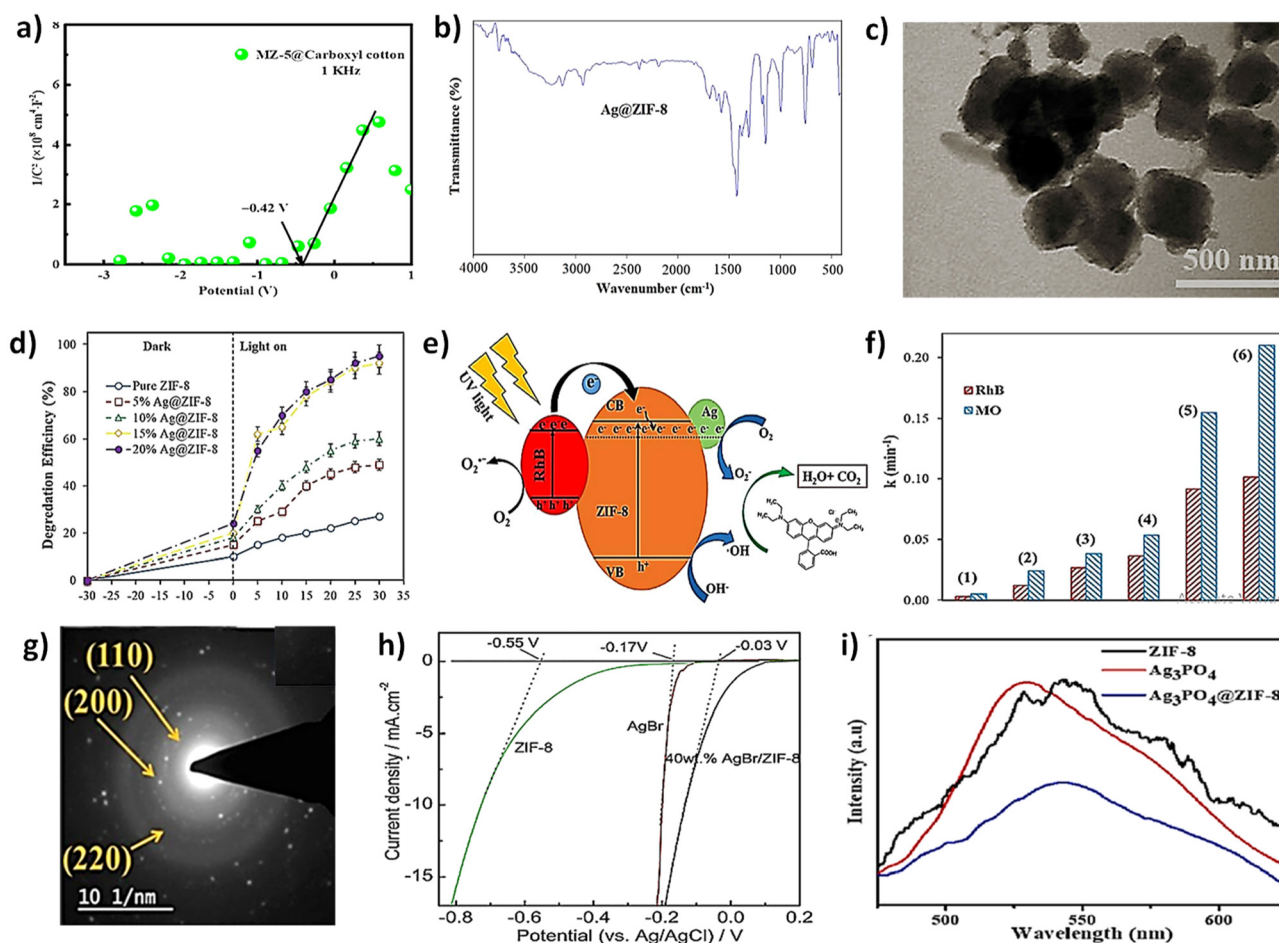


Fig. 7 (a) Mott–Schottky plots of MZ-5@Carboxyl cotton [reproduced from ref. 189 with the permission from Elsevier, copyright 2016]. (b) FTIR spectra of the prepared samples (Ag@ZIF-8 denotes 15% $Ag^+$ doped ZIF-8). (c) TEM images of Ag-15%@ ZIF-8 crystals. (d) Photodegradation performance of pure ZIF-8 and different amounts of Ag-doped ZIF-8 for eliminating RhB. (e) The proposed dye degradation mechanism of Ag@ZIF-8 photo-catalyst under visible-light irradiation [reproduced from ref. 176 with the permission from Elsevier, copyright 2020]. (f) Photodegradation first order rate constant of dyes by different samples in visible LED light: (1) without catalyst (only LED), (2) LED/$H_2O_2$, (3) pristine ZIF-8, (4) physical mixture of prior $AgNO_3$ and ZIF-8, (5) Ag-10%@ZIF-8, and (6) Ag-15%@ZIF-8 [reproduced from ref. 176 with the permission from Elsevier, copyright 2020]. (g) SEAD pattern of SZ2 [reproduced from ref. 177 with the permission from Elsevier, copyright 2020]. (h) LSV curves of ZIF-8, AgBr, and 40 wt% AgBr/ZIF-8 photocatalysts in 0.5 M $Na_2SO_4$ electrolyte [reproduced from ref. 191 with the permission from Elsevier, copyright 2019]. (i) PL spectra of ZIF-8, $Ag_3PO_4$, and $Ag_3PO_4$@ZIF-8 nanocomposite [reproduced from ref. 192 with the permission from Elsevier, copyright 2023].

Thanh *et al.* synthesized Fe-doped ZIF-8 with varying molar ratios of Zn/Fe and evaluated the photoinduced photocatalytic activity of the resulting materials for decomposing Remazol deep black B (RDB). The XRD analysis of Fe-doped ZIF-8 displayed the typical peaks of ZIF-8, with no detectable peaks for iron oxide. Nonetheless, the intensity of these peaks diminished as the iron content was increased. The peaks for Fe $2p_{3/2}$ were observed at 710 and 709 eV, suggesting the presence of Fe (II) and Fe(III). The $N_2$ adsorption/desorption isotherms for ZIF-8 and Fe-ZIF-8, both exhibiting type IV with H4 hysteresis, are typical of mesoporous materials. The Fe-ZIF-8 (1 : 9) sample displayed a slightly altered shape at high relative pressure, indicating structural distortion due to iron oxide incorporation. ZIF-8 had a specific surface area of 1484 $m^2$ $g^{-1}$, which decreased with iron addition to 1469, 1104, and 735 $m^2$ $g^{-1}$ for Fe-ZIF-8 (1 : 9), (2 : 8), and (3 : 7), respectively, confirming that iron oxide encapsulation reduced the accessible void space. To assess the sustainability of Fe-ZIF-8 for RDB removal, the used Fe-ZIF-8 was renewed by drying at 100 °C and then used again for photocatalytic decomposition of the RDB dye. After three cycles, the decolorization efficiency of Fe-ZIF-8 catalysts was 90–95% of that observed with the fresh catalysts.[193]

Jafar Abdi and team synthesized a porous Ag-doped ZIF-8 photocatalyst at ambient temperature using a facile and rapid synthesis. This catalyst was employed for the degradation of both MO and RhB dyes. The FTIR spectrum of Ag@ZIF-8 confirms that the ZIF-8 framework remains intact, with key absorption bands preserved. The broad band at 3400 $cm^{-1}$ and the band at 1633 $cm^{-1}$ correspond to the O–H stretching and bending vibrations, respectively. These hydroxyl groups, linked to adsorbed water, are essential for photocatalytic activity (Fig. 7b). ZIF-8 crystals possess a rhombic dodecahedron shape with a mesoporous structure. Fig. 7c demonstrates that Ag nanoparticles are well-dispersed throughout the ZIF-8 framework with little aggregation. The XRD spectrum of Ag@ZIF-8 shows preserved ZIF-8 peaks with no contaminants, while decreased intensity indicates Ag NP integration. EIS experiments revealed that the Ag-15%@ZIF-8 exhibited a narrower Nyquist plot arc radius compared with pure ZIF-8, reflecting enhanced light-induced charge migration and better exciton separation. This sample also illustrates the maximum photocatalytic efficiency, with first-order kinetic rate constants of 0.1016 $min^{-1}$ for RhB and 0.2102 $min^{-1}$ for MO. Photodegradation data (Fig. 7d) indicated that Ag NP enhanced dye removal. Increasing Ag content to 20 wt% improved performance, but higher doping did not yield further benefits. The rate constant (k) for decolorization was calculated using a first-order kinetic model (Fig. 7e). The Ag-15%@ZIF-8 photocatalyst mineralized over 93% of the dyes after 4 cycles (Fig. 7f). The photocatalytic efficiency of Ag-doped ZIF-8 was superior to that of a physical mixture of pure ZIF-8 and AgNO$_3$, because of the enhanced performance of the heterojunction formed between them.[176]

Silver (Ag) has garnered significant attention as a coupling material. Silver nanoparticles and compounds, including Ag$_3$VO$_4$, Ag$_2$O, Ag$_2$S, Ag$_3$PO$_4$, Ag$_2$CO$_3$, and particularly silver halides (AgX, where X = I, Br, and Cl), are extensively used for purifying organically contaminated wastewater through photocatalytic degradation.[194–198] The combination of elemental silver with silver halides enhances their activity in the visible light spectrum. Chandra *et al.* introduced a novel composite, ZIF8/AgNPs, designed for the photocatalytic degradation of MB. With its remarkable surface area of 1370.91 $m^2$ $g^{-1}$ and distinctive synergistic properties, the composites, labeled as SZ, SZ1, SZ2, and SZ3, varied in silver content. The size of the encapsulated silver NPs increased proportionally with their dosing amount. The crystalline nature of AgNPs, SZ2, and SZ composites was verified through the SEAD pattern depicted in Fig. 7g, respectively. Using the Tauc method, the band gap in all composites has been determined to be 5.27 eV and 5.13 eV, respectively, attributed to ZIF-8. However, the SZ composite, which contains a significant amount of Ag NPs, shows a broad band at 2.16 eV and 1.62 eV. This is because of the Ag and the imidazole ring interactions. Notably, SZ2, synthesized using a 300 mL suspension of Ag NPs, exhibited exceptional photocatalytic efficiency, achieving a 97.25% degradation rate for MB and complete degradation for CR at pH ≥ 7, while SZ, SZ1, SZ3, and ZIF-8 can decompose off 85.56, 90.56, 86.43 and 84.18% MB and 98.09, 96.18, 97.7 and 95.80% CR. This clearly illustrates the greatly improved photocatalytic performance of SZ2 and the superior activity of SZ1 compared with ZIF-8.[177]

Silver halide photocatalysts, recognized for their strong visible light response and exceptional photoactivity, have attracted considerable interest from researchers. AgX (X = Cl, Br, I) has been confirmed as an effective co-catalyst. In this context, He and colleagues described the synthesis of a ZIF-8/AgBr composite through the solvothermal method, utilized for the light-activated degradation of MB under light exposure. The SEM image of 40 wt% AgBr/ZIF-8 reveals AgBr particles randomly distributed on the ZIF-8 surface, a finding confirmed by EDS analysis. Optical analysis demonstrated enhanced light absorption capacity due to the combination of ZIF-8 and AgBr. Moreover, a bathochromic shift in the spectral absorption band was observed with higher AgBr content. The LSV curves in 0.5 M Na$_2$SO$_4$ show that AgBr exhibits a greater electrical density than ZIF-8, aligning with the PC results. The 40 wt% of the composite further enhances the electrical density, highlighting the synergistic impact of AgBr and ZIF-8 on electron transfer (Fig. 7h). The improved efficiency in charge separation stemmed from the synergistic impact of ZIF-8 and AgBr coupling. The recorded rate of MB degradation was 0.0273 $min^{-1}$, and the degradation performance achieved 99.5% under visible light exposure for 60 minutes. Stability and recyclability tests revealed that the 40 wt% of AgBr/ZIF-8 photocatalyst demonstrated reliable photocatalytic performance, maintaining its effectiveness through six repeated cycles.[191]

A study by Liu and his group demonstrated that the effect of incorporating ZIF-8 on the photocatalytic activity of Ag/AgCl was discussed. Initially, Ag/AgCl NPs were incorporated on the ZIF-8 surface with a 50 wt% loading, resulting in the synthesis of a (50%) Ag/AgCl/ZIF-8 composite. This hybrid displayed significant absorption of 420–800 nm in the wavelength range

due to the SPR phenomenon of Ag particles generated *in situ* on the surface of AgCl nanoparticles. In comparison with Ag/AgCl alone, the composite demonstrated excellent photocatalytic performance, attributed to the bifunctional activity of ZIF-8: adsorption of RhB and production of superoxide species, contributing to RhB mineralization. The photocatalytic efficiency of the hybrid in degrading MB was calculated without catalyst, with ZIF-8 alone, and with Ag/AgCl@ZIF-8 under UV light. Without a catalyst, MB degradation reached 67.31% over 90 min, while ZIF-8 alone exhibited limited improvement, achieving 51.53% degradation after 60 min of UV irradiation. In contrast, Ag/AgCl@ZIF-8 showed remarkable performance, achieving nearly 100% degradation within 20 min of UV exposure, despite minimal removal (9.25%) in the dark. The study concluded that while ZIF-8 alone had marginal effects, Ag/AgCl@ZIF-8 significantly increased photocatalytic performance, primarily attributed to improved photocatalysis.[178]

Guan *et al.* prepared a composite material composed of Ag/AgCl/ZIF-8/TiO$_2$/C on cotton fabric using a straightforward method. The Ag/AgCl/ZIF-8/TiO$_2$/C photocatalyst achieved a methylene blue degradation activity of 98.5% in 1 h 45 minutes under visible light, exhibiting a first-order kinetic rate constant of 0.0332 min$^{-1}$. Additionally, the photocatalyst maintained an 85% degradation efficiency of MB after three cycles, indicating its excellent stability. They demonstrated that the ZIF-8 in the composite promoted oxygen molecules throughout the photocatalytic decomposition, and photogenerated holes in the photocatalyst's VB oxidized water molecules to OH, resulting in the formation of hydroxyl OH$^{\bullet}$ and O$_2^{\bullet-}$, which were the active species liable for the photodegradation of MB during this process.[199]

Silver orthophosphate (Ag$_3$PO$_4$), a p-type semiconductor, has garnered significant attention in organic pollutant remediation through impressive visible light capture.[200] Considering this, Motora *et al.* synthesized a novel Ag$_3$PO$_4$@ZIF-8 p–n heterojunction using the chemical precipitation method at ambient temperature. The photocatalytic efficiency of this new photocatalyst was assessed for organic pollutants, including Congo Red, Crystal violet, and rhodamine B. The Ag$_3$PO$_4$@ZIF-8 heterojunction displayed distinct peaks for both Ag$_3$PO$_4$ and ZIF-8, with no extra peaks detected, verifying that the heterojunction was successfully synthesized without any impurities. The PL spectra in Fig. 7i demonstrated that the Ag$_3$PO$_4$@ZIF-8 heterojunction had lower PL intensity, indicating reduced charge carrier recombination. Furthermore, the photoinduced current demonstrated that the Ag$_3$PO$_4$@ZIF-8 heterojunction revealed the greatest photocurrent among ZIF-8 and Ag$_3$PO$_4$, indicating superior light absorption. This suggests remarkable electron–hole separation and reduced electron–hole recombination, which improves the photocatalytic activity of the heterojunction. Furthermore, the EIS semicircle radius for the Ag$_3$PO$_4$@ZIF-8 heterojunction was lower than Ag$_3$PO$_4$ and ZIF-8, reflecting enhanced current-carrying capacity, which is critical for effective photocatalysis. The developed photocatalyst showed exceptional photocatalytic

activity, degrading 90.7% of CV, 94.7% of CR, and 99.0% of RhB within 2 hours. The reusability of the photocatalyst, which is crucial for its practical application, was also examined. The Ag$_3$PO$_4$@ZIF-8-5% heterojunction demonstrated superior cyclic stability over five cycles, verifying its strong potential for real-world wastewater treatment applications.[192]

CQDs are fluorescent nanomaterials with a carbon framework and nanocrystals sized 2–10 nm. They are valued for low toxicity, high biocompatibility, tunable luminescence, and easy modification, making them a promising candidate for photocatalysis due to their fluorescence emission across the near-infrared to blue spectrum. Taking these aspects, Si *et al.* employed an impregnation method in which ZIF-8 structures were modified with carbon quantum dots and evaluated for their ability to remove methylene blue from water. The ultra-high resolution confocal laser scanning microscope (CLSM) image reveals the external morphology of CQDs@ZIF-8. CQDs emit fluorescence between 450 and 470 nm. It shows their distribution within ZIF-8, confirming the successful construction of the core–shell structure. The ZIF-8@CQD hybrid demonstrated a higher absorption capacity and improved responsiveness to visible light due to its core–shell structure, achieving a 91% removal activity for MB and a rate constant that was six times higher than that of ZIF-8 alone. Furthermore, the ZIF-8@CQD photocatalyst maintained excellent structural stability and catalytic activity over three reuse cycles without any loss of performance.[183]
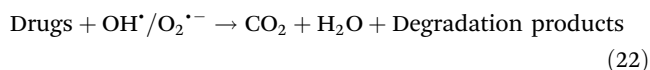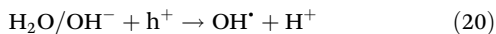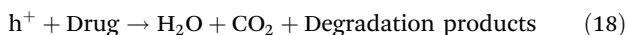
Studies indicate that combining ZIF-8 with materials such as graphitic carbon nitride, and zinc oxide not only boosts the degradation rates but also enhances the reusability and durability of the photocatalysts. Investigating the underlying mechanisms of charge transfer and degradation pathways in these composites could also provide deeper insights and lead to the improvement of more efficient and versatile photocatalytic systems for various environmental applications.

### 4.5 Drug degradation

The photocatalytic degradation of drugs involves three key steps: photon absorption, excitation, and reaction. Photogenerated carriers separate and migrate to the photocatalyst surface, where they trigger secondary reactions with adsorbed substances. Photogenerated holes can directly degrade drugs. There are two primary degradation pathways: a reductive pathway, which occurs if the conduction band (CB) potential is negative relative to the O$_2$/O$_2^{\bullet-}$ redox potential (−0.13 eV *vs.* RHE), and in this pathway, photoexcited electrons react with O$_2$ to produce superoxide radicals (O$_2^{\bullet-}$); and an oxidative pathway, where holes on the photocatalyst surface generate hydroxyl radicals ($^{\bullet}$OH) from H$_2$O/OH$^-$, depending on the pH of the medium. Hydrogen ions can recombine with electrons, producing heat and decreasing photodegradation efficiency. The photocatalyst's redox potential needs to be greater than $^{\bullet}$OH/OH$^-$ (+1.99 eV *vs.* RHE). Reactive radicals ($^{\bullet}$OH and O$_2^{\bullet-}$) can mineralize antibiotics and their intermediates into carbon dioxide and water under extended UV exposure. Both pathways work together to prevent electron

accumulation in the CB and reduce electron–hole recombination more effectively than direct interaction pathways.[201–204]

$$\text{Photocatalyst} \xrightarrow{h\vartheta} \text{Photocatalyst} + h^+ + e^- \qquad (17)$$

$$h^+ + \text{Drug} \rightarrow H_2O + CO_2 + \text{Degradation products} \qquad (18)$$

$$O_2 + e^- \rightarrow O_2^{\bullet -} \qquad (19)$$

$$H_2O/OH^- + h^+ \rightarrow OH^\bullet + H^+ \qquad (20)$$

$$H^+ + e^- \rightarrow \text{energy} \qquad (21)$$

$$\text{Drugs} + OH^\bullet/O_2^{\bullet -} \rightarrow CO_2 + H_2O + \text{Degradation products} \qquad (22)$$

Metal oxides are widely used in photocatalysis due to their metal content. $TiO_2$ is considered an excellent photocatalyst for its non-toxic nature, cost-effectiveness, and high efficiency. Li *et al.* synthesized ZIF-8@$TiO_2$ microcomposites *via* a hydrothermal method. The composite retains a dodecahedron shape with textured surfaces. Vibrational peaks at 565 cm$^{-1}$ and 486 cm$^{-1}$ correspond to N–Ti–O and Ti–O–Ti bonds, indicating $TiO_2$ deposition on ZIF-8 through chemical bonding rather than physical mixing (Fig. 8a). XPS confirms Ti$^{4+}$ binding with ZIF-8's imidazole groups to form N–Ti–O bonds, while EDX mapping shows Ti and O elements dispersed on

ZIF-8@$TiO_2$. Under 40 minutes of irradiation, ZIF-8@$TiO_2$ achieves a TC degradation rate of ~90%, surpassing $TiO_2$ and ZIF-8 (<70%). Trapping experiments revealed $O_2^{\bullet -}$ as the key reactive species, with benzoquinone (BQ) reducing degradation from 95% to 59%. Other species, such as OH and e$^-$, played minor roles. The effectiveness order was: no scavenger > IPA > CCl$_4$ > AO > BQ, confirming $O_2^{\bullet -}$ as the most crucial active species. The reusability and stability of the ZIF-8@$TiO_2$ composite across five degradation cycles, the TC removal rate decreased slightly from 95% to 86%, likely due to the loss of photocatalyst during recovery. This outcome shows that the ZIF-8@$TiO_2$ composite exhibits strong stability and reusability, with its internal interactions ensuring sustained high efficiency.[93]

$Cu_2O$, with a bandgap of 1.8–2.2 eV, is affordable, eco-friendly, and effective under visible light. Zhou *et al.* developed $Cu_2O$/ZIF-8 (C/Z) *via* an *in situ* growth method. XRD confirmed the synthesis of $Cu_2O$ and ZIF-8, while XPS identified key elements: N 1s (398.7 eV) confirmed the N–C bond, with Cu$^+$ peaks at 951.8 eV and 932 eV, and Zn 2p peaks at 1021.5 eV and 1044.7 eV (Fig. 8b). The C/Z composite demonstrated improved photocatalytic performance for tetracycline (TC) degradation because of the narrow bandgap of $Cu_2O$ and the increased surface area of ZIF-8, which is 3.3 times greater than $Cu_2O$ alone, offering increased adsorption sites. This led to a
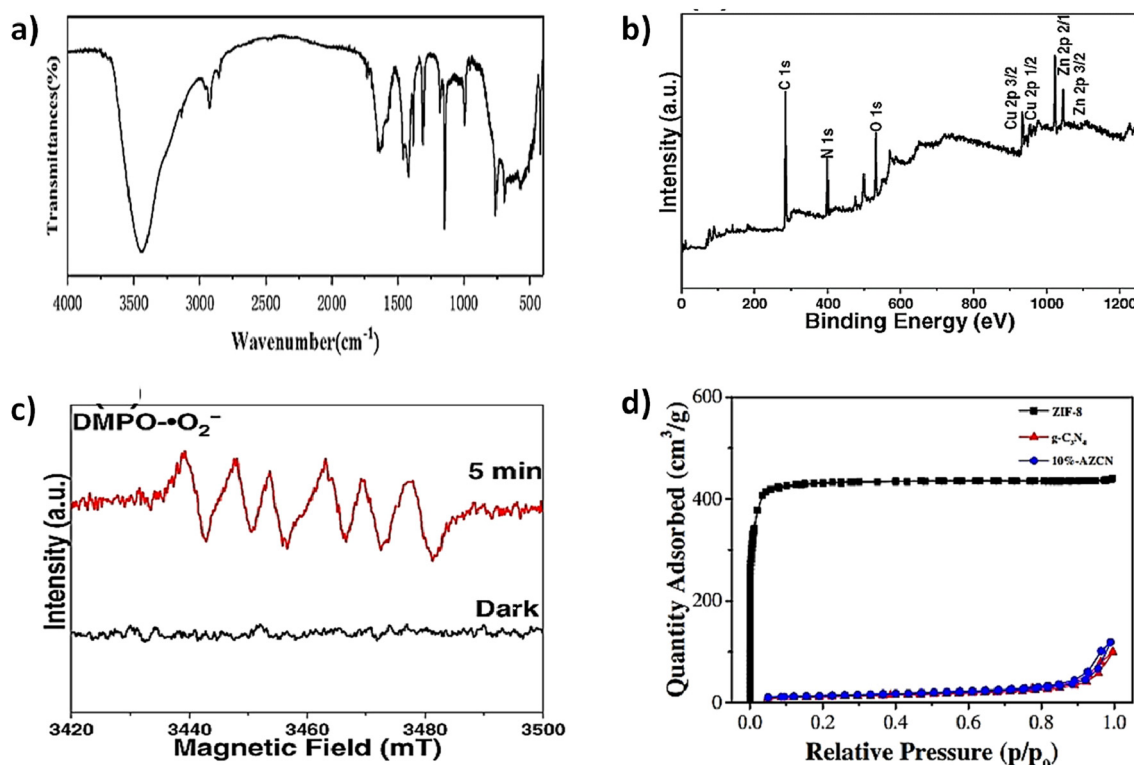


**Fig. 8** (a) FTIR spectra of ZIF-8@$TiO_2$ [reproduced from ref. 93 with the permission from Elsevier, copyright 2020]. (b) XPS survey spectra of C0.7/Z0.3 sample. (c) ESR spectra of DMPO-$O_2$ of the $Cu_2O$, ZIF-8 and C0.7/Z0.3 [reproduced from ref. 166 with the permission from Elsevier, copyright 2021]. (d) $N_2$ adsorption–desorption isotherm of ZIF-8, g-$C_3N_4$, ZIF-8 and 10%-AZCN samples [reproduced from ref. 169 with the permission from Elsevier, copyright 2019].
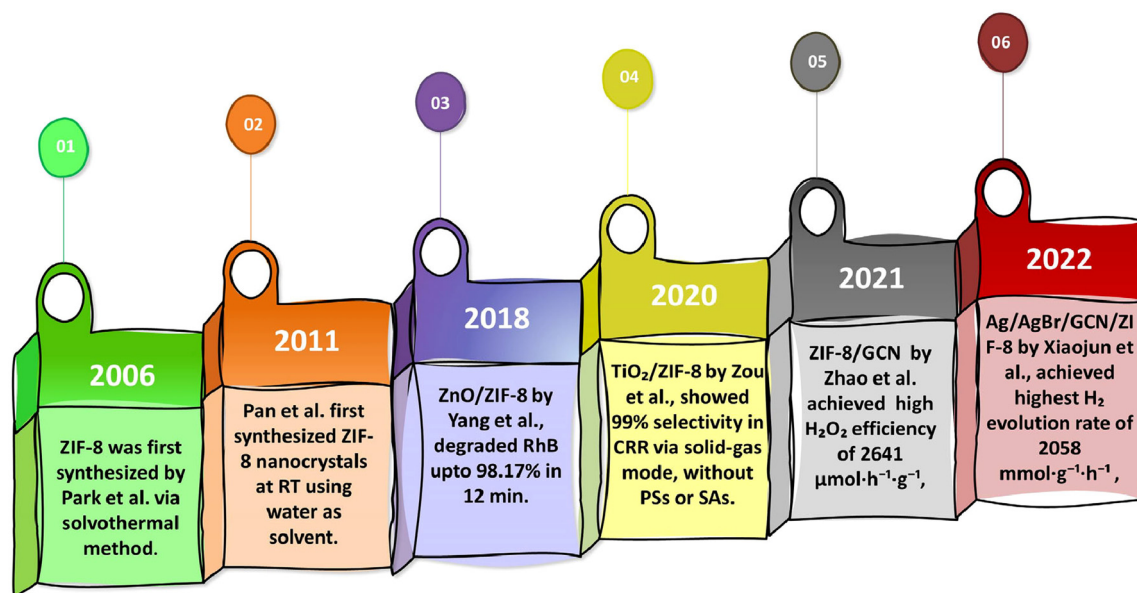
**Fig. 9** Development history of ZIF–8 MOFs and their nanocomposites as photocatalysts.

higher response to visible light and greater charge carrier density compared with individual components. The composite also showed superior photocurrent density and charge transfer efficiency, as indicated by a smaller semicircle diameter in the Nyquist plot. ESR analysis confirmed the generation of free radicals during photocatalysis, with $O_2{}^{\cdot-}$ being the primary radical, supported by weaker $\cdot OH$ signals (Fig. 8c). The C/Z composite achieved over 84.1% TC degradation under visible light within 2 hours, with efficiency slightly decreasing to 75.4% after four cycles. Additionally, the removal rates of TC, oxytetracycline, and tetracycline hydrochloride under visible light were 84.1%, 52.2%, and 73.5%, respectively.[166]

Graphitic carbon nitride, having a band gap of 2.7 eV, enhanced the reactive sites and the performance of carrier separation in the photocatalyst. The combination of Ag/AgCl@ZIF-8 with g-C₃N₄ successfully addressed both the extensive band gap of ZIF-8 and the limited surface area of g-C₃N₄. As previously mentioned, Fan *et al.* prepared an Ag/AgCl@ZIF-8 composite that demonstrated superb photocatalytic performance.[178] Furthermore, Zhou *et al.* modified this composite by loading g-C₃N₄ (AZCN) onto its surface to remove levofloxacin (LVFX) by using the facile stirring method. The homogeneous distribution of Ag, Zn, C, N, and Cl validates the successful synthesis of the composite by TEM EDX mapping. The optical characteristics of the photocatalysts were evaluated by UV–vis DRS (Fig. 8d), where g-C₃N₄ shows an absorption edge around 440 nm in the visible region, while ZIF's absorption edge is at 246 nm. The Ag/AgCl@ZIF-8 sample exhibits an absorption range from 300 to 800 nm. The PL spectra, where the 10%-AZCN sample exhibits the smallest peak intensity, indicate that the optimal ratio of Ag/AgCl@ZIF-8 to g-C₃N₄ enhances photoelectron transfer effectiveness and maximizes photocatalytic activity. LC-MS

measurement revealed that the AZCN composite, in conjunction with PMS, effectively breaks down LVFX into smaller molecules by sequentially eliminating diverse functional groups, ultimately oxidizing it to $CO_2$ and $H_2O$. In addition to photocatalysis, advanced oxidation processes (AOPs) were used in drug wastewater purification. Peroxymonosulfate (PMS) can produce $SO_4{}^{\cdot-}$ radicals when activated by other reactive species. These radicals oxidize most contaminants and assist other reactive species in the synergistic degradation of LVFX. Without PMS, AZCN achieved only a 53.6% degradation rate for LVFX.[169]

The photocatalytic degradation of drugs using ZIF-8-based composites reveals their potential through effective photon absorption and reactive radical generation. Integrating ZIF-8 with various materials enhances photocatalytic performance by improving charge carrier dynamics and radical production, leading to higher degradation rates for various drugs, such as tetracycline and levofloxacin. Future work should focus on refining these composites and exploring new materials to address diverse drug contaminants and improve practical applications in wastewater treatment.

## 5. Conclusion

Despite their relatively brief development history, ZIFs have garnered significant attention, leading to numerous achievements in recent years. ZIF-8-based materials are increasingly utilized in energy generation and wastewater treatment due to their catalytic activity and high porosity. This review provides in-depth overviews and analysis of the synthesis and applications of ZIF-8-based photocatalysts and their composites in light-mediated $H_2$ evolution, $H_2O_2$ evolution, $CO_2$ reduction, and pollutant removal. ZIF-8 has unique potential for develop-

ing alternative photocatalysts due to their exceptional properties, including effective charge separation, abundant active sites, and persistent porosity. Constructing catalyst composites from ZIF-8 and other functional materials offers several advantages for photocatalytic implementations over traditional single catalyst methods. Photoactive semiconductors or molecules in the composite enhance ZIF-8 solar light utilization. ZIF-8-based composites, with their high surface areas, provide active sites, prevent nanoparticle aggregation, and act as electron acceptors for charge carrier separation. Strong interfacial connections between ZIF-8 and semiconductors harvest visible light enhance electron transfer. As a result, ZIF-8-based composites typically demonstrate much greater photocatalytic efficiency compared with catalysts that consist of only one component. Currently, there is substantial interest in developing ZIF-8-based photocatalysts for environmental remediation and energy production that remain stable in the complex while being cost-effective and environmentally friendly. Although this field has made significant progress, much work remains before these photocatalysts can be widely applied (Fig. 9). However, more research is necessary to make ZIF-8 composite components viable for extensive photocatalytic application, as they are currently expensive, and we believe that current studies only scratch the surface of their potential. Our reasoning is based on the following points:

I. Most ZIF-based materials are microporous, with pore diameters less than 2 nm. This can limit their effectiveness, particularly when dealing with larger pollutant molecules due to steric hindrance. Therefore, it is beneficial to synthesize hierarchically porous materials from ZIFs that incorporate a range of pore sizes, including mesopores, macropores, and micropores.

II. Numerous synthetic techniques have been developed for both research and large-scale production of ZIF-8, yet achieving controlled synthesis with high crystallinity and uniform size remains difficult. Uniform size and crystallinity are crucial for application performance, especially in small-scale devices and electron conduction applications.

III. ZIF-8 has relatively low water stability due to the susceptibility of its coordination bonds to water. Enhancing the long-term water stability of ZIF-8 in a cost-effective manner continues to be a significant challenge.

IV. The chemical and thermal stability of ZIF-8-based composites must be carefully addressed for industrial implementations. Additionally, the catalytic sites and porosity should be managed skilfully.

V. Solar-active ZIF-8-based composites for hydrogen evolution could significantly contribute to renewable global energy solutions. However, ZIF-8 has a broadband gap, restricting its potential for solar energy utilization. Therefore, an adjustment approach to enhance sensitivity to visible light in both pristine ZIF-8 and its composites is crucial. Incorporating plasmonic materials can be advantageous, but it is essential to keep the cost-effectiveness in check.

VI. Multiple reaction parameters, such as temperature, ionic strength, and pH, are analyzed to assess their impact on pollutant degradation performance. Exploring the relationship between these variables and the effectiveness of ZIF-8 composites is essential to provide valuable references for the most effective synthesis and reaction parameters. This is crucial for the rational fabrication of adsorbents and photocatalysts. Furthermore, ZIF-8 composites must maintain long-term stability in various environmental conditions and be produced cost-effectively for industrial applications. Research should aim to improve solar light absorption efficiency, lower the rate of electron–hole pair recombination, and consider the recyclability of these materials as also important for practical applications.

VII. Photodegradation of organic contaminants using ZIF-8 and its composites is a highly emerging technology for pollution control owing to its low cost and eco-friendly nature. Currently, most research focuses on dye degradation, like RB, MB, and MO. However, there is a need to broaden the scope to include a wider range of organic impurities, such as perfluorinated organic chemicals (PFCs), along with pharmaceutical and personal care products (PPCPs) to better evaluate the photocatalytic decomposition capabilities of these components. It has been recommended to use actual polluted water rather than simulated wastewater and to measure the degradation efficiency by assessing the total organic carbon (TOC) removal percentage along with the highest absorbance of the targeted pollutant. Additionally, to advance toward industrial applications, extensive research is needed to understand the factors influencing photocatalytic efficiency, including co-existing ions, dissolved organic matter, and pH levels.

VIII. Numerous questions concerning the underlying mechanisms still require thorough clarification. In particular, the photocatalytic processes, including the separation of charge carriers generated by light and charge migration within multi-constituent systems, remain insufficiently understood for certain synthesized materials. Gaining a deeper insight into these catalytic mechanisms is crucial for developing next-generation photocatalysts with superior photocatalytic performance. To achieve this, integrating *in situ* characterization methods combined with theoretical simulations might be essential to clarify these mechanisms.

IX. The reclaimability of photocatalysts from aqueous solutions is vital for practical applications. Most ZIF-8/ZIF-8-based composite photocatalysts are solid powders that, despite being stable in aqueous solutions, have a diffusive nature that makes them challenging to separate from the reaction solution for recycling. It is significant to enhance novel ZIF-8/ZIF-8-based composite materials that can be more easily separated from solutions, such as forming films/membranes or shaping them into pellets/monoliths. Additionally, toxicity analyses have not yet been undertaken, which is vital for their resilient use.

X. A wide range of ZIF-8 composites have been developed, and even small variations in synthesis conditions can lead to significantly different properties. Despite continuous advancements in characterization technologies, examining the interface between ZIF-8 and the incorporated materials remains essential. *In situ* techniques like SEM, TEM, FTIR, and XPS are commonly employed to study the formation of ZIF-8 compo-
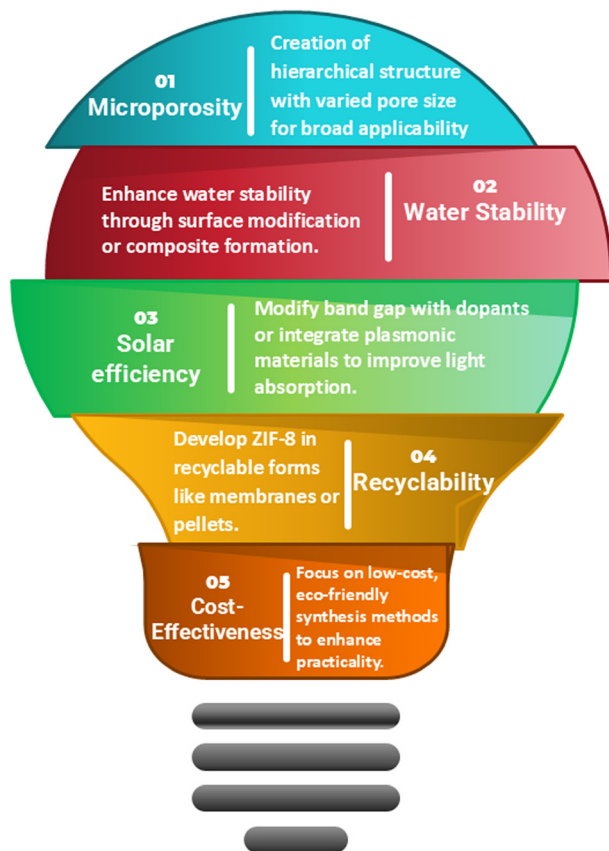
**Fig. 10** Schematic representation of challenges and future research directions toward ZIF-8-based nanomaterials for photocatalytic applications.

sites. Future research should, therefore, aim to explore the synergistic mechanisms of these composites using advanced analytical methods.

XI. Lastly, eco-friendly ZIF-8-based materials are essential for widespread practical applications in energy production and water treatment. The environmentally friendly properties are crucial from a pragmatic standpoint. Therefore, greater emphasis should be placed on achieving a low production-cost ratio while using biocompatible constituents (Fig. 10).

## Author contributions

Diptirani Behera: conceptualization, writing – original draft, visualization. Priyanka Priyadarshini: conceptualization, writing – original draft editing and review. Kulamani Parida: conceptualization, visualization, supervision.

## Data availability

The submitted review article synthesizes and discusses data that have already been published and are publicly available from the sources cited in the manuscript. No new data were generated during the preparation time frame of this review.

## Conflicts of interest

There are no conflicts to declare.

## Acknowledgements

## References

1 P. Raizada, P. Shandilya, P. Singh and P. Thakur, *J. Taibah Univ. Sci.*, 2017, **11**, 689–699.

2 P. Singh, K. Sharma, V. Hasija, V. Sharma, S. Sharma, P. Raizada, M. Singh, A. K. Saini, A. Hosseini-Bandegharaei and V. K. Thakur, Elsevier Ltd, 2019, preprint, DOI: **10.1016/j.mtchem.2019.08.005**.

3 V. Hasija, A. Sudhaik, P. Raizada, A. Hosseini-Bandegharaei and P. Singh, *J. Environ. Chem. Eng.*, 2019, **7**, 103272.

4 S. Bolisetty, M. Peydayesh and R. Mezzenga, Royal Society of Chemistry, 2019, preprint, DOI: **10.1039/c8cs00493e**.

5 M. S. Rahaman, H. Thérien-Aubin, M. Ben-Sasson, C. K. Ober, M. Nielsen and M. Elimelech, *J. Mater. Chem. B*, 2014, **2**, 1724–1732.

6 S. Patial, V. Hasija, P. Raizada, P. Singh, A. A. P. Khan Singh and A. M. Asiri, *J. Environ. Chem. Eng.*, 2020, **8**, 103791.

7 P. Thakur, P. Raizada, P. Singh, A. Kumar, A. A. P. Khan and A. M. Asiri, *Arabian J. Chem.*, 2020, **13**, 8271–8300.

8 K. Sharma, P. Raizada, A. Hosseini-Bandegharaei, P. Thakur, R. Kumar, V. K. Thakur, V. H. Nguyen and S. Pardeep, *Process Saf. Environ. Prot.*, 2020, **142**, 63–75.

9 L. Biswal, S. P. Tripathy, S. Dash, S. Das, S. Subudhi and K. Parida, *Mater. Adv.*, 2024, **5**, 4452–4466.

10 M. A. Shannon, P. W. Bohn, M. Elimelech, J. G. Georgiadis, B. J. Mariñas and A. M. Mayes, *Science and technology for water purification in the coming decades*, 2009.

11 A. Rahmani-Sani, P. Singh, P. Raizada, E. Claudio Lima, I. Anastopoulos, D. A. Giannakoudakis, S. Sivamani, T. A. Dontsova and A. Hosseini-Bandegharaei, *Bioresour. Technol.*, 2020, **297**, 122452.

12 P. Raizada, A. Sudhaik and P. Singh, KeAi Communications Co., 2019, preprint, DOI: **10.1016/j.mset.2019.04.007**.

13 P. Raizada, S. Sharma, A. Kumar, P. Singh, A. A. P. Khan and A. M. Asiri, *J. Environ. Chem. Eng.*, 2020, **8**, 104230.

14 S. Malato, P. Fernández-Ibáñez, M. I. Maldonado, J. Blanco and W. Gernjak, 2009, preprint, DOI: **10.1016/j. cattod.2009.06.018**.

15 H. Choi, M. G. Antoniou, A. A. de la Cruz, E. Stathatos and D. D. Dionysiou, *Desalination*, 2007, **202**, 199–206.

16  S. Nayak, K. Kumar Das and K. Parida, *J. Colloid Interface Sci.*, 2023, **634**, 121–137.

17  S. K. Sahoo, L. Acharya, L. Biswal, P. Priyadarshini and K. Parida, Royal Society of Chemistry, 2024, preprint, DOI: **10.1039/d4qi00950a**.

18  H. Huang, L. Jiang, J. Yang, S. Zhou, X. Yuan, J. Liang, H. Wang, H. Wang, Y. Bu and H. Li, *Renewable Sustainable Energy Rev.*, 2023, **173**, 113110.

19  J. Yang, H. Wang, L. Jiang, H. Yu, Y. Zhao, H. Chen, X. Yuan, J. Liang, H. Li and Z. Wu, *Chem. Eng. J.*, 2022, **427**, 130991.

20  A. Mishra, N. Priyadarshini, S. Mansingh and K. Parida, *Adv. Colloid Interface Sci.*, 2024, 103300.

21  J. Sahu, D. Prusty, S. Mansingh and K. Parida, Elsevier Ltd, 2023, preprint, DOI: **10.1016/j.ijhydene.2023.04.109**.

22  S. Tuckute, S. Varnagiris, M. Urbonavicius, M. Lelis and S. Sakalauskaite, *Appl. Surf. Sci.*, 2019, **489**, 576–583.

23  H. Yi, M. Yan, D. Huang, G. Zeng, C. Lai, M. Li, X. Huo, L. Qin, S. Liu, X. Liu, B. Li, H. Wang, M. Shen, Y. Fu and X. Guo, *Appl. Catal., B*, 2019, **250**, 52–62.

24  M. W. Kadi, R. M. Mohamed and A. A. Ismail, *Ceram. Int.*, 2020, **46**, 8819–8826.

25  S. Sa-nguanprang, A. Phuruangrat, T. Thongtem and S. Thongtem, *Inorg. Chem. Commun.*, 2020, **117**, 107944.

26  K. S. Bhavsar, P. K. Labhane, R. B. Dhake and G. H. Sonawane, *Chem. Phys. Lett.*, 2020, **744**, 137202.

27  G. J. Lee and J. J. Wu, Elsevier B.V., 2017, preprint, DOI: **10.1016/j.powtec.2017.05.022**.

28  S. B. Atla, W. R. Lin, T. C. Chien, M. J. Tseng, J. C. Shu, C. C. Chen and C. Y. Chen, *Mater. Chem. Phys.*, 2018, **216**, 380–386.

29  J. Carbajo, M. Jiménez, S. Miralles, S. Malato, M. Faraldos and A. Bahamonde, *Chem. Eng. J.*, 2016, **291**, 64–73.

30  Sonu, V. Dutta, S. Sharma, P. Raizada, A. Hosseini-Bandegharaei, V. Kumar Gupta and P. Singh, Elsevier B.V., 2019, preprint, DOI: **10.1016/j.jscs.2019.07.003**.

31  J. Sahu, S. Mansingh, B. P. Mishra, D. Prusty and K. Parida, *Dalton Trans.*, 2023, **52**, 16525–16537.

32  W. K. Fan and M. Tahir, Elsevier Ltd, 2022, preprint, DOI: **10.1016/j.enconman.2021.115180**.

33  Y. Li, H. Xu, S. Ouyang and J. Ye, Royal Society of Chemistry, 2016, preprint, DOI: **10.1039/c5cp05885f**.

34  S. Dash, S. P. Tripathy, S. Subudhi, L. Acharya, A. Ray, P. Behera and K. Parida, *Energy Adv.*, 2024, **3**, 1073–1086.

35  A. Phan, C. J. Doonan, F. J. Uribe-Romo, C. B. Knobler, M. Okeeffe and O. M. Yaghi, *Acc. Chem. Res.*, 2010, **43**, 58–67.

36  O. M. Yaghi, N. W. Ockwig, H. K. Chae, M. Eddaoudi and J. Kim, *Reticular synthesis and the design of new materials*, 2003.

37  K. Li, Y. Zhang, Y. Z. Lin, K. Wang and F. T. Liu, *ACS Appl. Mater. Interfaces*, 2019, **11**, 28918–28927.

38  P. Priyadarshini and K. Parida, Elsevier Ltd, 2024, preprint, DOI: **10.1016/j.est.2024.111379**.

39  J. Ran, H. Zeng, J. Cai, P. Jiang, P. Yan, L. Zheng, Y. Bai, X. Shen, B. Shi and H. Tong, *Chem. Eng. J.*, 2018, **333**, 20–33.

40  Y. Liu, Z. Zhu, X. Pei, X. Zhang, X. Cheng, S. Hu, X. Gao, J. Wang, J. Chen and Q. Wan, *ACS Appl. Mater. Interfaces*, 2020, **12**, 36978–36995.

41  M. Ahmad, M. Yousaf, W. Cai and Z. P. Zhao, *Chem. Eng. J.*, 2023, **453**, 139846.

42  X. Tang, J. H. Zhao, Y. H. Li, Z. J. Zhou, K. Li, F. T. Liu and Y. Q. Lan, *Dalton Trans.*, 2017, **46**, 10553–10557.

43  A. Karakeçili, B. Topuz, S. Korpayev and M. Erdek, *Mater. Sci. Eng., C*, 2019, **105**, 110098.

44  L. Jiao, J. Y. R. Seow, W. S. Skinner, Z. U. Wang and H. L. Jiang, Elsevier B.V., 2019, preprint, DOI: **10.1016/j. mattod.2018.10.038**.

45  H. Kaur, G. C. Mohanta, V. Gupta, D. Kukkar and S. Tyagi, *J. Drug Delivery Sci. Technol.*, 2017, **41**, 106–112.

46  A. Dhakshinamoorthy, Z. Li and H. Garcia, Royal Society of Chemistry, 2018, preprint, DOI: **10.1039/c8cs00256h**.

47  W. Zhen, B. Li, G. Lu and J. Ma, *Chem. Commun.*, 2015, **51**, 1728–1731.

48  V. Pascanu, G. González Miera, A. K. Inge and B. Martín-Matute, American Chemical Society, 2019, preprint, DOI: **10.1021/jacs.9b00733**.

49  S. R. Batten, B. Chen and J. J. Vittal, *ChemPubSoc.*, 2016, **81**, 669–670.

50  Y. V. Kaneti, S. Dutta, M. S. A. Hossain, M. J. A. Shiddiky, K. L. Tung, F. K. Shieh, C. K. Tsung, K. C. W. Wu and Y. Yamauchi, *Adv. Mater.*, 2017, **29**, 1700213.

51  T. He, Z. Huang, S. Yuan, X. L. Lv, X. J. Kong, X. Zou, H. C. Zhou and J. R. Li, *J. Am. Chem. Soc.*, 2020, **142**, 13491–13499.

52  P. Behera, A. Ray, S. P. Tripathy, L. Acharya, S. Subudhi and K. Parida, *J. Photochem. Photobiol., A*, 2023, **436**, 114415.

53  L. Jiang, S. Zhou, J. Yang, H. Wang, H. Yu, H. Chen, Y. Zhao, X. Yuan, W. Chu and H. Li, *Adv. Funct. Mater.*, 2022, **32**, 2108977.

54  P. A. Desario and K. A. Gray, in *Metropolitan Sustainability: Understanding and Improving the Urban Environment*, Elsevier Ltd, 2012, pp. 292–316.

55  M. P. M. Dicker, P. F. Duckworth, A. B. Baker, G. Francois, M. K. Hazzard and P. M. Weaver, Elsevier Ltd, 2014, preprint, DOI: **10.1016/j.compositesa.2013.10.014**.

56  Z. C. Kong, J. F. Liao, Y. J. Dong, Y. F. Xu, H. Y. Chen, D. Bin Kuang and C. Y. Su, *ACS Energy Lett.*, 2018, **3**, 2656–2662.

57  A. Chakraborty, D. A. Islam and H. Acharya, *J. Solid State Chem.*, 2019, **269**, 566–574.

58  X. Liu, J. Zhang, Y. Dong, H. Li, Y. Xia and H. Wang, *New J. Chem.*, 2018, **42**, 12180–12187.

59  K. S. Park, Z. Ni, A. P. Cô, J. Y. Choi, R. Huang, F. J. Uribe-Romo, H. K. Chae, M. O'keeffe and O. M. Yaghi, *Exceptional chemical and thermal stability of zeolitic imidazolate frameworks*, 2006.

60  Y. Pan, Y. Liu, G. Zeng, L. Zhao and Z. Lai, *Chem. Commun.*, 2011, **47**, 2071–2073.

61  Y. Song, C. Yu, D. Ma and K. Liu, Elsevier B.V., 2024, preprint, DOI: **10.1016/j.ccr.2023.215492**.

62 K. Shalini, K. Sharma and N. Kumar, *Der Chemica Sinica*, 2011, **7**, 668–677.

63 P. Molina, A. Tárraga and F. Otón, 2012, preprint, DOI: **10.1039/c2ob06808g**.

64 A. Jayashree, B. Narayana, S. M. Kumar, K. R. Raghi, B. K. Sarojini and T. K. M. Kumar, *Chem. Data Collect.*, 2019, **21**, 100237.

65 H. Bux, F. Liang, Y. Li, J. Cravillon, M. Wiebcke and J. Caro, *J. Am. Chem. Soc.*, 2009, **131**, 16000–16001.

66 H. Wu, W. Zhou and T. Yildirim, *J. Am. Chem. Soc.*, 2007, **129**, 5314–5315.

67 J. B. James and Y. S. Lin, *J. Membr. Sci.*, 2017, **532**, 9–19.

68 H. Yin, H. Kim, J. Choi and A. C. K. Yip, *Chem. Eng. J.*, 2015, **278**, 293–300.

69 W. Zhou, H. Wu, M. R. Hartman and T. Yildirim, *J. Phys. Chem. C*, 2007, **111**, 16131–16137.

70 Y. Song, M. He, J. Zhao and W. Jin, Elsevier B.V., 2021, preprint, DOI: **10.1016/j.seppur.2021.118722**.

71 S. Naghdi, M. M. Shahrestani, M. Zendehbad, H. Djahaniani, H. Kazemian and D. Eder, Elsevier B.V., 2023, preprint, DOI: **10.1016/j.jhazmat.2022.130127**.

72 B. Chen, Z. Yang, Y. Zhu and Y. Xia, Royal Society of Chemistry, 2014, preprint, DOI: **10.1039/c4ta02984d**.

73 A. U. Ortiz, A. P. Freitas, A. Boutin, A. H. Fuchs and F. X. Coudert, *Phys. Chem. Chem. Phys.*, 2014, **16**, 9940–9949.

74 S. K. Nune, P. K. Thallapally, A. Dohnalkova, C. Wang, J. Liu and G. J. Exarhos, *Chem. Commun.*, 2010, **46**, 4878–4880.

75 X. C. Huang, Y. Y. Lin, J. P. Zhang and X. M. Chen, *Angew. Chem., Int. Ed.*, 2006, **45**, 1557–1559.

76 S. R. Venna and M. A. Carreon, *J. Am. Chem. Soc.*, 2010, **132**, 76–78.

77 A. X. Zhu, R. B. Lin, X. L. Qi, Y. Liu, Y. Y. Lin, J. P. Zhang and X. M. Chen, *Microporous Mesoporous Mater.*, 2012, **157**, 42–49.

78 K. Milburn and H. Zhang, *Synthesis and Characterization of ZIF-8 and ZIF-8/polymer composites*, 2014.

79 A. Kumar, S. Rana, G. Sharma, P. Dhiman, M. I. Shekh and F. J. Stadler, Elsevier Ltd, 2023, preprint, DOI: **10.1016/j.jece.2023.110770**.

80 Y. Wang, Y. Xu, D. Li, H. Liu, X. Li, S. Tao and Z. Tian, *Chin. J. Catal.*, 2015, **36**, 855–865.

81 Y. Liu, H. Cheng, M. Cheng, Z. Liu, D. Huang, G. Zhang, B. Shao, Q. Liang, S. Luo, T. Wu and S. Xiao, Elsevier B.V., 2021, preprint, DOI: **10.1016/j.cej.2020.127914**.

82 L. Tian, X. Yang, Q. Liu, F. Qu and H. Tang, *Appl. Surf. Sci.*, 2018, **455**, 403–409.

83 J. Cravillon, C. A. Schröder, H. Bux, A. Rothkirch, J. Caro and M. Wiebcke, *CrystEngComm*, 2012, **14**, 492–498.

84 J. Cravillon, R. Nayuk, S. Springer, A. Feldhoff, K. Huber and M. Wiebcke, *Chem. Mater.*, 2011, **23**, 2130–2141.

85 M. He, J. Yao, L. Li, K. Wang, F. Chen and H. Wang, *ChemPlusChem*, 2013, **78**, 1222–1225.

86 H. Song, N. Wang, H. Meng, Y. Han, J. Wu, J. Xu, Y. Xu, X. Zhang and T. Sun, *Dalton Trans.*, 2020, **49**, 10816–10823.

87 Y. Pan and Z. Lai, *Chem. Commun.*, 2011, **47**, 10275–10277.

88 B. Ding, X. Wang, Y. Xu, S. Feng, Y. Ding, Y. Pan, W. Xu and H. Wang, *J. Colloid Interface Sci.*, 2018, **519**, 38–43.

89 V. V. Butova, A. P. Budnyk, E. A. Bulanova, C. Lamberti and A. V. Soldatov, *Solid State Sci.*, 2017, **69**, 13–21.

90 R. Oozeerally, S. D. K. Ramkhelawan, D. L. Burnett, C. H. L. Tempelman and V. Degirmenci, *Catalysts*, 2019, **9**, 100812.

91 Y. Hong, B. Wang, S. Hu, S. Lu, Q. Wu, M. Fu, C. Gu and Y. Wang, *Ceram. Int.*, 2023, **49**, 11027–11037.

92 A. Faraji, N. Mehrdadi, N. M. Mahmoodi, M. Baghdadi and A. Pardakhti, *J. Mol. Struct.*, 2021, **1223**, 129028.

93 R. Li, W. Li, C. Jin, Q. He and Y. Wang, *J. Alloys Compd.*, 2020, **825**, 154008.

94 E. R. Parnham and R. E. Morris, *Acc. Chem. Res.*, 2007, **40**, 1005–1013.

95 R. E. Morris, 2008, preprint, DOI: **10.1002/anie.200704888**.

96 E. R. Cooper, C. D. Andrews, P. S. Wheatley, P. B. Webb, P. Wormald and R. E. Morris, *Nature*, 2004, **430**, 1012–1016.

97 G. A. V. Martins, P. J. Byrne, P. Allan, S. J. Teat, A. M. Z. Slawin, Y. Li and R. E. Morris, *Dalton Trans.*, 2010, **39**, 1758–1762.

98 W. J. Son, J. Kim, J. Kim and W. S. Ahn, *Chem. Commun.*, 2008, 6336–6338.

99 K. S. Suslick, P. F. Schubert, R. E. J. Johnson, Amer, W. Tsang, A. Lifshitz, E. Lewis, N. F. Golden, D. M. Smith, G. P. Fujikawa, S. Akamatsu, T. Chendke and P. K. Fogler, *1980, 97, 481. E 2i*, McGraw-Hill, 1986, vol. 108.

100 B. Seoane, J. M. Zamaro, C. Tellez and J. Coronas, *CrystEngComm*, 2012, **14**, 3103–3107.

101 H. Y. Cho, J. Kim, S. N. Kim and W. S. Ahn, *Microporous Mesoporous Mater.*, 2013, **169**, 180–184.

102 M. Schlesinger, S. Schulze, M. Hietschold and M. Mehring, *Microporous Mesoporous Mater.*, 2010, **132**, 121–127.

103 P. da and F. FRANCESCO Coordinatore Dottorato Relatore Aldo Roda Dario Braga, Alma Mater Studiorum-Università di Bologna DOTTORATO DI RICERCA IN CHIMICA Ciclo XXIX Synthesis and characterization of new luminescent complexes based on Copper(ɪ) Iodide.

104 C. J. Adams, M. A. Kurawa and A. G. Orpen, *Dalton Trans.*, 2010, **39**, 6974–6984.

105 C. J. Adams, H. M. Colquhoun, P. C. Crawford, M. Lusi and A. G. Orpen, *Angew. Chem., Int. Ed.*, 2007, **46**, 1124–1128.

106 P. J. Beldon, L. Fábián, R. S. Stein, A. Thirumurugan, A. K. Cheetham and T. Friščić, *Angew. Chem.*, 2010, **122**, 9834–9837.

107 D. Braga, M. Curzi, A. Johansson, M. Polito, K. Rubini and F. Grepioni, *Angew. Chem., Int. Ed.*, 2005, **45**, 142–146.

108 T. Friščić, D. G. Reid, I. Halasz, R. S. Stein, R. E. Dinnebier and M. J. Duer, *Angew. Chem., Int. Ed.*, 2010, **49**, 712–715.

109 T. Friščić, I. Halasz, P. J. Beldon, A. M. Belenguer, F. Adams, S. A. J. Kimber, V. Honkimäki and R. E. Dinnebier, *Nat. Chem.*, 2013, **5**, 66–73.

110 S. Tanaka, K. Kida, T. Nagaoka, T. Ota and Y. Miyake, *Chem. Commun.*, 2013, **49**, 7884–7886.

111 M. Li and M. Dincă, *J. Am. Chem. Soc.*, 2011, **133**, 12926–12929.

112 T. Zhang, J. Z. Wei, X. J. Sun, X. J. Zhao, H. Liang Tang, H. Yan and F. M. Zhang, *Inorg. Chem. Commun.*, 2020, **111**, 107671.

113 O. J. De Lima Neto, A. C. de O. Frós, B. S. Barros, A. F. De Farias Monteiro and J. Kulesza, *New J. Chem.*, 2019, **43**, 5518–5524.

114 A. Martinez Joaristi, J. Juan-Alcañiz, P. Serra-Crespo, F. Kapteijn and J. Gascon, *Cryst. Growth Des.*, 2012, **12**, 3489–3498.

115 S. D. Worrall, H. Mann, A. Rogers, M. A. Bissett, M. P. Attfield and R. A. W. Dryfe, *Electrochim. Acta*, 2016, **197**, 228–240.

116 Z. Li, J. Cui, Y. Liu, J. Li, K. Liu and M. Shao, *ACS Appl. Mater. Interfaces*, 2018, **10**, 34494–34501.

117 L. Jiang, D. Zhou, J. Yang, S. Zhou, H. Wang, X. Yuan, J. Liang, X. Li, Y. Chen and H. Li, *J. Mater. Chem. A*, 2022, **10**, 13651–13672.

118 R. Wei, N. Tang, L. Jiang, J. Yang, J. Guo, X. Yuan, J. Liang, Y. Zhu, Z. Wu and H. Li, Elsevier B.V., 2022, preprint, DOI: 10.1016/j.ccr.2022.214500.

119 C. Mottillo and T. Friščić, MDPI AG, 2017, preprint, DOI: 10.3390/molecules22010144.

120 N. Kaur, M. Singh, A. Moumen, G. Duina and E. Comini, MDPI AG, 2020, preprint, DOI: 10.3390/ma13132974.

121 H.-C. Oh, S. Jung, I.-J. Ko and E.-Y. Choi, *Ionothermal Synthesis of Metal–Organic Framework*, 2016.

122 B. Kołodziej, *Pol. J. Chem. Technol.*, 2024, **4**, 39–55.

123 P. E. Lokhande, U. S. Chavan and A. Pandey, Springer Science and Business Media B.V., 2020, preprint, DOI: 10.1007/s41918-019-00057-z.

124 S. Subudhi, S. P. Tripathy and K. Parida, Royal Society of Chemistry, 2021, preprint, DOI: 10.1039/d0qi01117g.

125 X. Fang, Q. Shang, Y. Wang, L. Jiao, T. Yao, Y. Li, Q. Zhang, Y. Luo and H. L. Jiang, *Adv. Mater.*, 2018, **30**, 1705112.

126 C. Acar, I. Dincer and G. F. Naterer, John Wiley and Sons Ltd, 2016, preprint, DOI: 10.1002/er.3549.

127 P. Xing, F. Zhou and S. Zhan, *Environ. Res.*, 2021, **197**, 111167.

128 K. Suda and M. Nagata, in ECS Meeting Abstracts, 2020, vol. MA2020-02, pp. 3115–3115.

129 X. Chang, Y. Wang, X. Zhou, Y. Song and M. Zhang, *Dalton Trans.*, 2021, **50**, 17618–17624.

130 M. Zhang, Q. Shang, Y. Wan, Q. Cheng, G. Liao and Z. Pan, *Appl. Catal., B*, 2019, **241**, 149–158.

131 Y. Zhao, Y. Liu, J. Cao, H. Wang, M. Shao, H. Huang, Y. Liu and Z. Kang, *Appl. Catal., B*, 2020, **278**, 119289.

132 F. He, G. Chen, Y. Zhou, Y. Yu, L. Li, S. Hao and B. Liu, *J. Mater. Chem. A*, 2016, **4**, 3822–3827.

133 X. Dai, S. Feng, W. Zheng, W. Wu, Y. Zhou, Z. Ye, X. Cao and Y. Wang, *Int. J. Hydrogen Energy*, 2022, **47**, 10603–10615.

134 M. U. Shahid, T. Najam, M. H. Helal, I. Hossain, S. M. El-Bahy, Z. M. El-Bahy, A. ur Rehman, S. S. A. Shah and M. A. Nazir, Elsevier Ltd, 2024, preprint, DOI: 10.1016/j.ijhydene.2024.03.139.

135 R. Ren, H. Zhao, X. Sui, X. Guo, X. Huang, Y. Wang, Q. Dong and J. Chen, *Catalysts*, 2019, **9**, 89.

136 M. Zeng, Z. Chai, X. Deng, Q. Li, S. Feng, J. Wang and D. Xu, *Nano Res.*, 2016, **9**, 2729–2734.

137 S. Feng, Y. Yu, J. Li, J. Luo, P. Deng, C. Jia, Y. Shen and X. Tian, *Catal. Commun.*, 2022, **162**, 106382.

138 J. Joo, T. Kim, J. Lee, S. Il Choi and K. Lee, Wiley-VCH Verlag, 2019, preprint, DOI: 10.1002/adma.201806682.

139 Z. Jin and Y. Zhang, *Catal. Surv. Asia*, 2020, **24**, 59–69.

140 J. Chen, J. Chen and Y. Li, *J. Mater. Chem. A*, 2017, **5**, 24116–24125.

141 J. Zhou, J. Zhao and R. Liu, *Appl. Catal., B*, 2020, **278**, 119265.

142 J. H. Zhao, Y. Wang, X. Tang, Y. H. Li, F. T. Liu, Y. Zhang and K. Li, *Dalton Trans.*, 2019, **48**, 3560–3565.

143 X. Yuan, S. Qu, X. Huang, X. Xue, C. Yuan, S. Wang, L. Wei and P. Cai, *Chem. Eng. J.*, 2021, **416**, 129148.

144 M. R. Saleh, H. M. El-Bery and H. N. Abdelhamid, *Appl. Organomet. Chem.*, 2023, **37**, e6995.

145 X. Han, T. Zhang, Y. Cui, Z. Wang, R. Dong, Y. Wu, C. Du, R. Chen, C. Yu, J. Feng, J. Sun and S. Dong, *Molecules*, 2023, **28**, 2422.

146 S. Kato, J. Jung, T. Suenobu and S. Fukuzumi, *Energy Environ. Sci.*, 2013, **6**, 3756–3764.

147 D. Tsukamoto, A. Shiro, Y. Shiraishi, Y. Sugano, S. Ichikawa, S. Tanaka and T. Hirai, *ACS Catal.*, 2012, **2**, 599–603.

148 H. Hirakawa, S. Shiota, Y. Shiraishi, H. Sakamoto, S. Ichikawa and T. Hirai, *ACS Catal.*, 2016, **6**, 4976–4982.

149 Y. Xie, Y. Li, Z. Huang, J. Zhang, X. Jia, X. S. Wang and J. Ye, *Appl. Catal., B*, 2020, **265**, 118581.

150 X. Yang, Z. Wen, Z. Wu and X. Luo, *Inorg. Chem. Front*, 2018, **5**, 687–693.

151 E. Karamian and S. Sharifnia, *J. CO₂ Util.*, 2016, **16**, 194–203.

152 Y. H. Zou, H. N. Wang, X. Meng, H. X. Sun and Z. Y. Zhou, *Nanoscale Adv.*, 2021, **3**, 1455–1463.

153 R. Chandra, S. Mukhopadhyay and M. Nath, *Mater. Lett.*, 2016, **164**, 571–574.

154 X. Yang, Z. Wen, Z. Wu and X. Luo, *Inorg. Chem. Front.*, 2018, **5**, 687–693.

155 R. N. Compton, P. W. Reinhardt and C. D. Cooper, *J. Chem. Phys.*, 1975, **63**, 3821–3827.

156 I. Ganesh, Elsevier Ltd, 2014, preprint, DOI: 10.1016/j.rser.2013.11.045.

157 A. Corma and H. Garcia, *J. Catal.*, 2013, **308**, 168–175.

158 C. C. Yang, J. Vernimmen, V. Meynen, P. Cool and G. Mul, *J. Catal.*, 2011, **284**, 1–8.

159 J. Mao, T. Peng, X. Zhang, K. Li and L. Zan, *Catal. Commun.*, 2012, **28**, 38–41.

160 Z. Wang, X. Liu, A. Zhang, H. Zhao, H. Dong, H. Jia and B. Xu, *J. Inorg. Organomet. Polym. Mater.*, 2024, **34**, 4594–4608.

161 Y. Liu, L. Deng, J. Sheng, F. Tang, K. Zeng, L. Wang, K. Liang, H. Hu and Y. N. Liu, *Appl. Surf. Sci.*, 2019, **498**, 143899.

162 M. Izadpanah Ostad, M. Niknam Shahrak and F. Galli, *J. CO2 Util.*, 2021, **43**, 101373.

163 J. W. Maina, J. A. Schütz, L. Grundy, E. Des Ligneris, Z. Yi, L. Kong, C. Pozo-Gonzalo, M. Ionescu and L. F. Dumée, *ACS Appl. Mater. Interfaces*, 2017, **9**, 35010–35017.

164 Z. Huang, P. Dong, Y. Zhang, X. Nie, X. Wang and X. Zhang, *J. CO₂ Util.*, 2018, **24**, 369–375.

165 H. J. Peng, P. Q. Zheng, H. Y. Chao, L. Jiang and Z. P. Qiao, *RSC Adv.*, 2019, **10**, 551–555.

166 Y. Zhou, S. Feng, X. Duan, W. Wu, Z. Ye, X. Dai, Y. Wang and X. Cao, *J. Solid State Chem.*, 2022, **305**, 122628.

167 X. Lei, Y. Cao, Q. Chen, X. Ao, Y. Fang and B. Liu, *Colloids Surf., A*, 2019, **568**, 1–10.

168 W. Q. Chen, L. Y. Li, L. Li, W. H. Qiu, L. Tang, L. Xu, K. J. Xu and M. H. Wu, *Engineering*, 2019, **5**, 755–767.

169 J. Zhou, W. Liu and W. Cai, *Sci. Total Environ.*, 2019, **696**, 133962.

170 M. Cao, Z. Zhuang, Y. Liu, Z. Zhang, J. Xuan, Q. Zhang and W. Wang, *J. Colloid Interface Sci.*, 2022, **608**, 2779–2790.

171 N. M. Mahmoodi, S. Keshavarzi, M. Oveisi, S. Rahimi and B. Hayati, *J. Mol. Liq.*, 2019, **291**, 111333.

172 Y. Du, R. Z. Chen, J. F. Yao and H. T. Wang, *J. Alloys Compd.*, 2013, **551**, 125–130.

173 J. He, J. Ye, Y. Zhang, L. Kong, X. Zhou, Y. Ma and Y. Yang, *ChemistrySelect*, 2020, **5**, 3746–3755.

174 M. Ciprian, P. Xu, S. Chaemchuen, R. Tu, S. Zhuiykov, P. M. Heynderickx and F. Verpoort, *Microporous Mesoporous Mater.*, 2018, **267**, 185–191.

175 B. Abdollahi, A. Najafidoust, E. Abbasi Asl and M. Sillanpaa, *Arabian J. Chem.*, 2021, **14**, 103444.

176 J. Abdi, *Colloids Surf., A*, 2020, **604**, 125330.

177 R. Chandra and M. Nath, *J. Water Process Eng.*, 2020, **36**, 101266.

178 G. Fan, J. Luo, L. Guo, R. Lin, X. Zheng and S. A. Snyder, *Chemosphere*, 2018, **209**, 44–52.

179 N. Chang, Y. R. Chen, F. Xie, Y. P. Liu and H. T. Wang, *Colloids Surf., A*, 2021, **616**, 126351.

180 L. R. Jabbar and A. Al-Farraji, *Environ. Nanotechnol., Monit. Manage.*, 2022, **18**, 100701.

181 A. Malik, M. Nath, S. Mohiyuddin and G. Packirisamy, *ACS Omega*, 2018, **3**, 8288–8308.

182 M. Hu, H. Lou, X. Yan, X. Hu, R. Feng and M. Zhou, *Microporous Mesoporous Mater.*, 2018, **271**, 68–72.

183 Y. Si, X. Li, G. Yang, X. Mie and L. Ge, *J. Mater. Sci.*, 2020, **55**, 13049–13061.

184 I. B. S. Will, J. E. F. Moraes, A. C. S. C. Teixeira, R. Guardani and C. A. O. Nascimento, *Sep. Purif. Technol.*, 2004, **34**, 51–57.

185 M. H. Habibi and H. Vosooghian, *J. Photochem. Photobiol., A*, 2005, **174**, 45–52.

186 S. Bustos-Guadarrama, A. Nieto-Maldonado, L. Z. Flores-López, H. Espinoza-Gomez and G. Alonso-Nuñez, *J. Taiwan Inst. Chem. Eng.*, 2023, **142**, 104663.

187 C. Karunakaran, G. Abiramasundari, P. Gomathisankar, G. Manikandan and V. Anandi, *J. Colloid Interface Sci.*, 2010, **352**, 68–74.

188 O. İloğlu and H. A. Yurtsever, *Bitlis Eren Univ. Fen Bilimleri Derg.*, 2023, **12**, 764–772.

189 H. Chen, Y. Q. Wang, F. Huang, C. Tu and Li Cui, *Appl. Surf. Sci.*, 2021, **565**, 150458.

190 S. Das, L. Acharya, L. Biswal and K. Parida, *Nanoscale Adv.*, 2024, **6**, 934–946.

191 Y. He, L. Zeng, Z. Feng, Q. Zhang, X. Zhao, S. Ge, X. Hu and H. Lin, *Adv. Powder Technol.*, 2020, **31**, 439–447.

192 K. G. Motora, C. M. Wu and S. T. Lin, *J. Water Process Eng.*, 2023, **52**, 103586.

193 M. T. Thanh, T. V. Thien, P. D. Du, N. P. Hung and D. Q. Khieu, *J. Porous Mater.*, 2018, **25**, 857–869.

194 X. Hu and C. Hu, *J. Solid State Chem.*, 2007, **180**, 725–732.

195 T. Li, X. Hu, C. Liu, C. Tang, X. Wang and S. Luo, *J. Mol. Catal. A: Chem.*, 2016, **425**, 124–135.

196 S. Mohanty, P. Babu, K. Parida and B. Naik, *Inorg. Chem.*, 2019, **58**, 9643–9654.

197 H. Yu, W. Liu, X. Wang and F. Wang, *Appl. Catal., B*, 2018, **225**, 415–423.

198 W. M. Shume, H. C. A. Murthy and E. A. Zereffa, Hindawi Limited, 2020, preprint, DOI: **10.1155/2020/5039479**.

199 X. Guan, S. Lin, J. Lan, J. Shang, W. Li, Y. Zhan, H. Xiao and Q. Song, *Cellulose*, 2019, **26**, 7437–7450.

200 G. F. Huang, Z. L. Ma, W. Q. Huang, Y. Tian, C. Jiao, Z. M. Yang, Z. Wan and A. Pan, 2013, preprint, DOI: **10.1155/2013/371356**.

201 T. Velempini, E. Prabakaran and K. Pillay, Elsevier Ltd, 2021, preprint, DOI: **10.1016/j.mtchem.2020.100380**.

202 K. Qin, Q. Zhao, H. Yu, X. Xia, J. Li, S. He, L. Wei and T. An, *Environ. Res.*, 2021, **199**, 111360.

203 Y. Li, Y. Fu and M. Zhu, *Appl. Catal., B*, 2020, **260**, 118149.

204 X. Chen, J. Yao, B. Xia, J. Gan, N. Gao and Z. Zhang, *J. Hazard. Mater.*, 2020, **383**, 121220.